







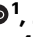




Deglacial release of petrogenic and permafrost carbon from the Canadian Arctic impacting the carbon cycle

Received: 11 September 2021

Accepted: 4 November 2022

Published online: 22 November 2022

 Check for updates

Junjie Wu^{1,6}  , Gesine Mollenhauer^{1,2}  , Ruediger Stein^{1,2,3}  , Peter Köhler¹ , Jens Hefter¹ , Kirsten Fahl¹ , Hendrik Grotheer¹ , Bingbing Wei⁴ & Seung-Il Nam⁵ 

The changes in atmospheric $p\text{CO}_2$ provide evidence for the release of large amounts of ancient carbon during the last deglaciation. However, the sources and mechanisms that contributed to this process remain unresolved. Here, we present evidence for substantial ancient terrestrial carbon remobilization in the Canadian Arctic following the Laurentide Ice Sheet retreat. Glacial-retreat-induced physical erosion of bedrock has mobilized petrogenic carbon, as revealed by sedimentary records of radiocarbon dates and thermal maturity of organic carbon from the Canadian Beaufort Sea. Additionally, coastal erosion during the meltwater pulses 1a and 1b has remobilized pre-aged carbon from permafrost. Assuming extensive petrogenic organic carbon oxidation during the glacial retreat, a model-based assessment suggests that the combined processes have contributed 12 ppm to the deglacial CO_2 rise. Our findings suggest potentially positive climate feedback of ice-sheet retreat by accelerating terrestrial organic carbon remobilization and subsequent oxidation during the glacial-interglacial transition.

Identifying Earth system processes that have contributed to atmospheric $p\text{CO}_2$ variability since the Last Glacial Maximum (LGM) remains one of the grand challenges in paleoclimatic research. During the last deglaciation, atmospheric CO_2 concentrations rose by ~ 75 ppm while the $\Delta^{14}\text{C}$ values of CO_2 declined^{1–3}. Evidence from both data and models suggests that the $p\text{CO}_2$ increase is driven mainly by changes in Southern Ocean ventilation, making the region a source of ancient carbon to the atmosphere^{4,5}. However, the oceanic CO_2 release alone cannot account for the full glacial/interglacial amplitude of CO_2 , or the rapid rise at 16.4, 14.6, and 11.5 cal. kyr BP, or the stable carbon isotopic anomaly of atmospheric CO_2 . Hence, terrestrial and marine carbon sources have been both invoked to explain the CO_2 variations^{6,7}.

Ice sheets have traditionally been regarded as an inert component in the carbon cycle and thus have not been considered to explain the CO_2 variations. Growing evidence of terrestrial carbon remobilization/oxidation related to ice-sheet retreat, however, has indicated the necessity of a careful re-evaluation of this paradigm^{8,9}. One can also imagine that glacial retreat directly leads to exposure to the atmosphere of organic carbon (OC) that has been isolated for many millennia and the oxidation of which may be important for the OC-rich regions. More recently, ice-sheet retreat and the subsequent exposure of its underlying shales have received attention to explain the CO_2 increases¹⁰.

¹Alfred-Wegener-Institut Helmholtz-Zentrum für Polar-und Meeresforschung (AWI), Bremerhaven 27568, Germany. ²MARUM—Center for Marine Environmental Sciences and Faculty of Geosciences, University of Bremen, Bremen 28359, Germany. ³Frontiers Science Center for Deep Ocean Multispheres and Earth System, and Key Laboratory of Marine Chemistry Theory and Technology, Ocean University of China, Qingdao 266100, China. ⁴State Key Laboratory of Marine Geology, Tongji University, Shanghai 200092, China. ⁵Korea Polar Research Institute, Incheon 21990, Republic of Korea. ⁶Present address: Department of Environmental Science, Stockholm University, Stockholm 11418, Sweden. ✉ e-mail: Junjie.Wu@aces.su.se; gesine.mollenhauer@awi.de; ru_st@uni-bremen.de

Oxidized petrogenic organic carbon (OC_{petro} ; rock-derived OC that is typically radiocarbon free) can be reintroduced into the active carbon cycle through chemical weathering or microbial utilization^{11,12}. Such processes have been proposed to regulate atmospheric CO_2 levels over geological timescales¹³. With more studies into this field, modern observations describe OC_{petro} oxidative weathering as a supply-limited process, oxidation flux depending on the rock erosion rate^{14,15}. High OC_{petro} supply is found in glaciated regions today and glacial denudation of bedrock is a significant contributor. In the southern Alps of New Zealand, the OC_{petro} oxidative weathering fluxes in glacier-dominated watersheds (up to $50 \text{ tC km}^{-2} \text{ yr}^{-1}$) are 2–3 times higher than those in less-glaciated watersheds¹⁵. Along the southeast Alaskan coast, the mass accumulation rates (MARs) of OC_{petro} in glaciated fjords are significantly higher than those in non-glaciated fjords¹⁶. Notably, initial evidence of enhanced OC_{petro} mobilization during the ice-sheet retreat has been seen in a sedimentary record obtained from the Bering Sea¹⁷. The above lines of evidence support rather substantial OC_{petro} mobilization for the previously glaciated continents and imply extensive OC_{petro} oxidation during the last deglaciation. It further raises questions, depending on the magnitude of carbon release, whether the processes are connected to the millennial-scale CO_2 increases during glacial terminations¹⁰.

During the LGM, much of northern North America was covered by the Laurentide Ice Sheet (LIS) and Cordilleran Ice Sheet^{18,19}. According to the underlying bedrock, northern North America can be subdivided into the OC_{petro} -rich western Canadian bedrock and the OC_{petro} -poor Canadian Shield. Ice-sheet retreat exposed the OC_{petro} -rich western Canadian bedrock during the last deglaciation²⁰, including shales, coal, and oil sands^{10,21}, and thus Blattmann¹⁰ hypothesized that bedrock exhumation and the subsequent OC_{petro} oxidation acted as a carbon source to the deglacial CO_2 rise. However, dedicated studies of this

process are still restricted in numbers and regions, and more work is required to test this hypothesis. Studying marine sediment cores archiving land-derived OC from this region may provide further insight into the relationship between glacial retreat and OC_{petro} remobilization during the last deglaciation.

Another terrestrial carbon pool that may be remobilized during the ice-sheet retreat is permafrost carbon, which has been freeze-locked for thousands of years and is vulnerable to degradation once thaws. Coastal erosion during the rapid sea-level rise, as a result of ice volume reduction, has been proposed to remobilize permafrost carbon and contribute to the deglacial CO_2 rise^{17,22–24}. However, so far, most studies on permafrost carbon remobilization have been carried out along the shelves or slopes of the Laptev Sea, the East Siberian Sea, the Chukchi Sea, the Bering Sea, the North Pacific, and the Okhotsk Sea^{17,23–27}. With the possible exception of the Bering Sea, the continental areas in the hinterland of these regions remained largely unglaciated during the LGM. Thus, a complex combination of processes during the last deglaciation, including water runoff, shelf flooding, and permafrost thawing in the interior, makes it difficult to unambiguously determine the process of coastal erosion. In contrast to the unglaciated regions, ice sheets in glaciated regions hindered vegetation development and the accumulation of carbon-rich permafrost deposits in the interior. This unique feature precludes signals from hinterland permafrost thawing and thus makes it an ideal region to study the process of coastal erosion.

Our study area in the Canadian Beaufort Sea is ideally located to elucidate both OC_{petro} mobilization and the process of coastal erosion during the last deglaciation. In this work, we analyze biomarker contents and radiocarbon signatures of sedimentary OC and of specific terrigenous biomarkers in core ARA04C/37 from the Canadian Beaufort Sea (Fig. 1), spanning the last 14 kyr²⁸. Another set of samples from

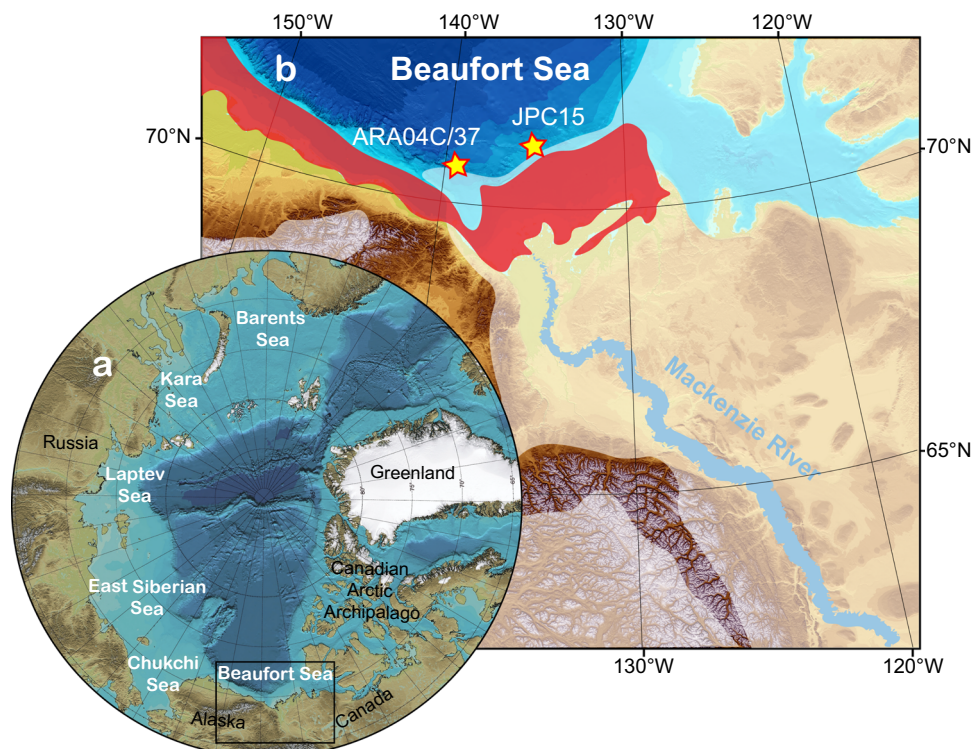


Fig. 1 | Overview of the Arctic Ocean and core locations in the Canadian Beaufort Sea. **a** overview of the Arctic Ocean and the study area (black box). **b** core locations of ARA04C/37 and JPC15 in this study are indicated by yellow stars and the Mackenzie River is outlined by a blue line. The red area between the paleo coast

and the present coastline has been flooded since the Last Glacial Maximum (ca. 21 cal. kyr BP), according to the global ICE-6G_C model⁴⁹. The white transparent areas indicate the Laurentide Ice Sheet extent during the Last Glacial Maximum¹⁹. The bathymetry is adapted from IBCAO Version 3.0⁶⁹.

nearby core JPC15²⁹ (Fig. 1) is analyzed to extend records into the Bølling/Allerød (B/A) interval. As ancient OC may consist of pre-aged terrestrial biospheric organic carbon ($OC_{terr-bio}$) and radiocarbon-free OC_{petro} , pyrolysis and biomarker proxies are used as supporting evidence of OC_{petro} contributions. We demonstrate that ice-sheet retreat has caused substantial OC_{petro} mobilization during the last deglaciation. Additionally, rapid sea-level rise at ca. 14 and 11 cal. kyr BP most likely caused two events of strong coastal erosion. Based on our findings, we attempt to estimate carbon release from OC_{petro} oxidation and assess the impacts of oxidized OC_{petro} and flooded permafrost on atmospheric carbon pools by using the global carbon cycle model BICYCLE³⁰. The simulations suggest that the two processes additively may have a long-term effect of an increase in atmospheric CO_2 of 12 ppm and a decrease in atmospheric $\Delta^{14}C$ of 12 permil.

Results

Glacial retreat mobilized substantial amounts of petrogenic OC

Today, the Mackenzie River is the largest river in the Canadian Arctic, with a water discharge of $316 \text{ km}^3 \text{ yr}^{-1}$ and sediment flux of $124\text{--}128 \text{ Mt yr}^{-1}$ (ref. 31). Strongly influenced by Mackenzie River input, sedimentary OC in this region is predominantly terrigenous. In core ARA04C/37, hydrogen index and oxygen index derived from Rock-Eval pyrolysis indicate a dominant terrestrial OC source throughout the records (Supplementary Fig. 1), which is in agreement with the low values of $\delta^{13}C_{org}$ between -28.5‰ and -25.5‰ (Fig. 2d)²⁸.

Radiocarbon dating of bulk OC is used to characterize carbon age at the time of deposition (pre-depositional age). The pre-depositional ages of bulk OC were oldest (20–30 kyrs) between 14.5–10 cal. kyr BP while values decreased throughout the Holocene (Fig. 2c). We note that some samples from the late B/A interval show a low ^{14}C content close to the background. The pre-depositional ages in these samples are reported as minimum ages (>30 kyrs). The OC delivered into the Canadian Beaufort Sea was much older between 14.5 and 10 cal. kyr BP compared to the Holocene input. When compared to the mean age of modern Mackenzie River particulate organic carbon (6.6 ± 1.2 kyrs) (ref. 32 and references therein), the differences are even larger.

Organic carbon in the modern Mackenzie River basin contains a large fraction of OC_{petro} ^{33,34}, and the increased carbon age may suggest an even increased OC_{petro} input in the past. Multiple proxies, i.e., carbon preference index of high molecular weight *n*-alkanes (CPI_{alk}), the fractional abundance of “biological” homohopane to its diagenetic isomers ($f\beta\beta$), and temperature at which pyrolysis yields the maximum of hydrocarbons (T_{max}), are used as support for large OC_{petro} input between 14.5–10 cal. kyr BP. These proxies have been proposed to indicate carbon thermal maturity (see methods) and thus are indicative of OC_{petro} input. However, as these proxies have limitations to specifically indicate OC_{petro} input, interpretation of their variations warrants caution. Nevertheless, the overall low values of CPI_{alk} and $f\beta\beta$, as well as high T_{max} values, are consistent with OC_{petro} input typical for the Mackenzie River basin and support increased OC_{petro} contribution between 14.5–10 cal. kyr BP (Fig. 2e–g). Hence, the largely increased carbon age is most likely attributed to the enhanced OC_{petro} contribution during the last deglaciation.

The period of enhanced OC_{petro} contribution (14.5–10 cal. kyr BP) coincides with finely laminated sediments (Fig. 2c, h, Supplementary Fig. 2), implying higher OC_{petro} MARs. The increased OC_{petro} MARs likely resulted from enhanced OC_{petro} supply. Glacial erosion and isostatic uplift due to the glacial retreat may have increased physical erosion of sedimentary rocks, resulting in a strongly enhanced OC_{petro} supply. The ice sheets, which entrained abraded material from the underlying rocks, including ancient kerogen deposits during the glaciation, may have released OC_{petro} upon melting. Besides, the possibly increased burial efficiency may have led to increased OC_{petro} MARs. In this study, burial efficiency is defined as the ratio between OC release

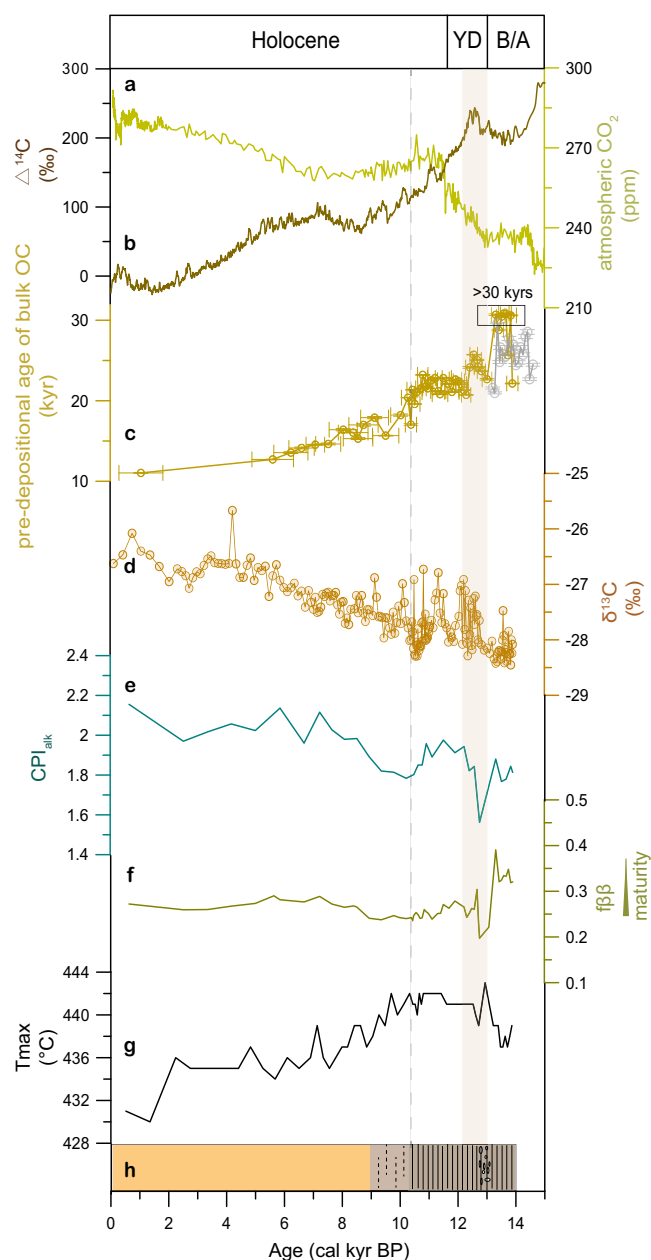


Fig. 2 Characteristics and thermal maturity of sedimentary organic matter in the Canadian Beaufort Sea. **a** atmospheric CO_2 concentrations⁷⁰; **b** radiocarbon content reconstructed in IntCal3⁶⁷; **c** pre-depositional age of bulk OC, brownish yellow for core ARA04C/37 and gray for core JPC15. Error bars represent standard deviation; **d** $\delta^{13}C_{org}$ values in core ARA04C/37²⁸; **e–g** thermal maturity proxies CPI_{alk} (carbon preference index of high molecular weight *n*-alkanes), $f\beta\beta$ (fractional abundance of “biological” homohopane to its diagenetic isomers), and T_{max} (temperature at which pyrolysis yields the maximum of hydrocarbons) of core ARA04C/37; **h** lithology and sedimentary texture (according to Supplementary Fig. 2), dark brown section indicates finely laminated sediments and orange section indicate bioturbated silty clay. The light brownish section with dashed lines represents the transition characterized by weakly laminated sediments. Abbreviations in the figure are defined as YD Younger Dryas, B/A Bølling/Allerød.

on land and its long-term burial in marine sediments. The factors that may have increased burial efficiency are discussed below (see Discussion).

Coastal erosion mobilized ancient permafrost carbon

The total organic carbon (TOC) MAR shows three distinct peaks during the last deglaciation and the early Holocene (Fig. 3d)²⁸.

The increased TOC MARs at the onset of the Younger Dryas (YD) can be explained by flood mobilization/transport of OC since multiple sedimentary records have documented the high-energy YD flood draining through the Mackenzie River to the Arctic Ocean (Fig. 3)^{28,29}. However, the other two events may have different causes. Although the ice-margin retreat in the Fort McMurray area and evidence of gravels and an erosion surface in the Canadian Arctic Coastal Plain together suggest a post-YD flood originating from the proglacial lakes McMurray, Meadow, and Churchill between 11.7–9.3 cal. kyr BP^{35,36}, so far, an unambiguous meltwater flood signal has not been identified in marine records. For instance, core JPC15 only documented the YD freshening ($\delta^{18}\text{O}$ -depleted water), while $\delta^{18}\text{O}$ values during the putative post-YD flood are even higher than 2‰ (Fig. 3a)²⁹, the baseline of the B/A interval which represents a deglacial environment of meltwater discharge. In core ARA04C/37, the terrestrial biomarkers branched glycerol dialkyl glycerol tetraethers (brGDGTs, most probably derived from proglacial lakes) and the diol proxy ($F_{\text{C}_{32}\ 1,15}$, indicative for running water) peaked during the YD flood, whereas no such clear signals were found during the post-YD flood (Fig. 3c, d), suggesting at least a less strong post-YD flood²⁸. Therefore, the increase in TOC MAR at ca. 11 cal. kyr BP cannot be fully explained by a post-YD flood. To better constrain the carbon sources which contributed to high TOC MARs at ca. 14 and 11 cal. kyr BP, more information about terrestrial carbon is needed.

The high molecular weight fatty acids (HMW-FAs) are synthesized by terrestrial higher plants and are widely found in plants and soils. Since they are expected to be largely absent in mature petrogenic materials, HMW-FAs are commonly taken to represent $\text{OC}_{\text{terr-bio}}$ ^{37–41}. The pre-depositional ages of HMW-FAs were the oldest (17–23 kyrs, with one age >30 kyrs) between 14.5 and 10 cal. kyr BP and values decreased during the Holocene (Fig. 3e). Furthermore, the ages of HMW-FAs during the last deglaciation exhibit large differences with modern $\text{OC}_{\text{terr-bio}}$ (5.8 ± 0.8 kyrs) in the Mackenzie River basin³⁴. Because the remobilized $\text{OC}_{\text{terr-bio}}$ is always a mixture of constituents of different carbon ages, e.g., young biospheric organic carbon synthesized by plants and pre-aged biospheric carbon from relic permafrost or deeper soil profiles, the older mean age of HMW-FAs likely indicates lower contributions from young constituents. This can be attributed to the fact that the LIS has restricted vegetation and reduced contributions from freshly produced biospheric carbon during the last deglaciation. It implies that the mean age of $\text{OC}_{\text{terr-bio}}$ during the last deglaciation is different from the modern one.

The pre-depositional ages of HMW-FAs were not uniformly old between 14.5 and 10 cal. kyr BP. Ages were much younger during the YD, indicating a younger inland $\text{OC}_{\text{terr-bio}}$ transported by freshwater discharge. However, the pre-depositional ages of HMW-FAs sharply increased at 14 and 11 cal. kyr BP (Fig. 3d, e). As permafrost formation along the Mackenzie River basin was restricted by the LIS and there was no obvious enhancement in ice melting, the very old HMW-FAs and rapidly increased TOC MARs were unlikely caused by hinterland permafrost thawing or glacial melting. Rather, the two events co-occurred with the global meltwater pulses (MWP) 1a and 1b (Fig. 3d–f), indicating that the old HMW-FAs have a most probable source from coastal permafrost and/or ancient OC-rich deposits, released by coastal erosion. The first erosion event occurred slightly after the MWP 1a at ca. 13.9–13.4 cal. kyr BP (Figs. 3e, f). Since the nearby core JPC15/27 with a total recovery of 13 m has documented very high sedimentation rates and laminated sediments between 14.4–13.5 cal. kyr BP (6–12 m)²⁹, it is likely that the slight apparent delay in our records is due to a lack of accelerator mass spectrometry (AMS) ^{14}C dates at the base of core ARA04C/37 (see methods) or an incomplete record of this event.

Although the distinct increases in TOC MAR were likely linked to coastal erosion during the MWP 1a and 1b, parameters of bulk OC, i.e.,

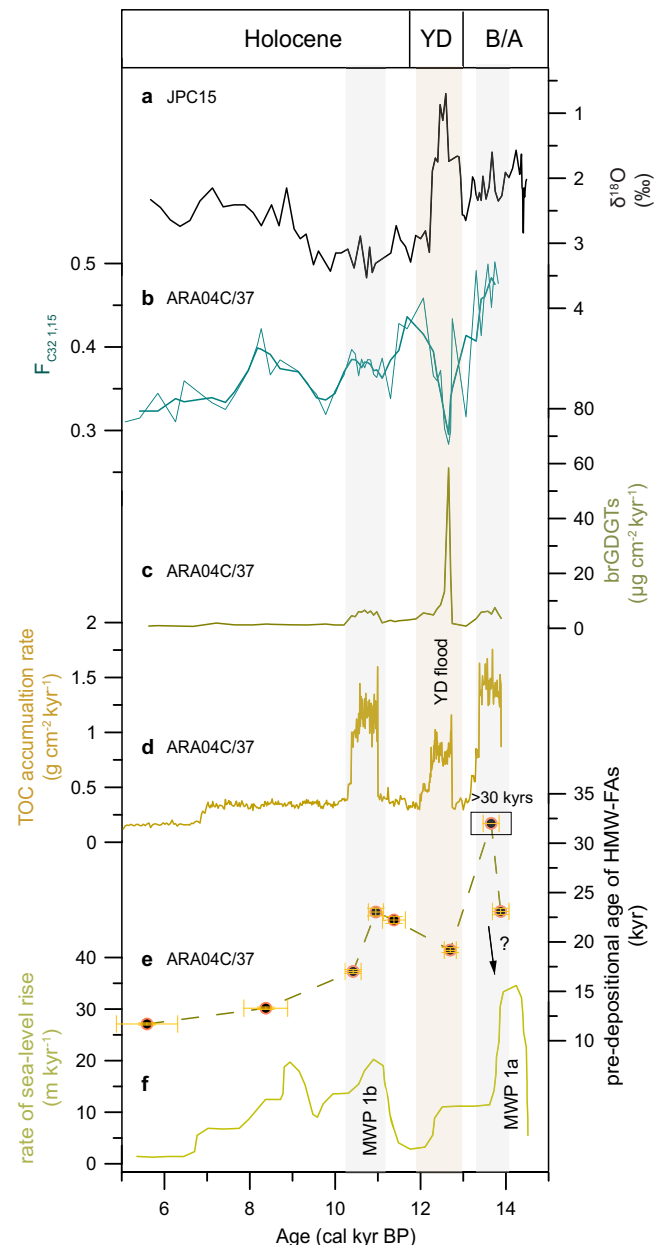


Fig. 3 | Coastal erosion and Younger Dryas flood event. **a** $\delta^{18}\text{O}$ values of *Neogloboquadrina pachyderma* in core JPC15²⁹; **b**, **c** $F_{\text{C}_{32}\ 1,15}$ (fractional abundance of $\text{C}_{32}\ 1,15$ -diol) and mass accumulation rate of brGDGTs (branched glycerol dialkyl glycerol tetraethers) in core ARA04C/37²⁸; **d** mass accumulation rate of TOC (total organic carbon)²⁸; **e** pre-depositional age of HMW-FAs (high molecular weight fatty acids). Horizontal error bars represent standard deviation, and vertical error bars represent the propagated uncertainties of the blank-corrected values; **f** rate of sea-level rise⁷¹. Abbreviations in the figure are defined as YD Younger Dryas, B/A Bølling/Allerød, MWP meltwater pulse.

$\delta^{13}\text{C}$, CPI, $\beta\beta$, and T_{max} did not show significant changes (Fig. 2). This suggests that, despite the strong coastal erosion, bulk OC was still dominated by OC_{petro} while remobilization of ancient $\text{OC}_{\text{terr-bio}}$ only accounted for small contributions. The overwhelming OC_{petro} input can be attributed to (1) continuously high OC_{petro} supply from the hinterland and (2) significant contributions from the eroded coastal deposits containing OC_{petro} debris⁴².

Discussion

The records of core ARA04C/37 present direct evidence for substantial remobilization of OC_{petro} following the LIS retreat.

Towards quantitative estimates, a three-endmember mixing model based on a Markov chain Monte Carlo Bayesian approach was used to apportion relative contributions of OC_{petro} , $OC_{\text{terr-bio}}$, and marine biospheric carbon (Fig. 4b). More information on endmembers, endmember values, and the mixing model can be found in the Supplementary Discussion. The OC_{petro} was estimated to contribute ~50–80% of TOC during the last deglaciation, and its relative contribution decreased to ~20–50% in the late Holocene (Fig. 4a, Supplementary Table 1). The estimated fraction in the late Holocene is close to the modern observations at the Mackenzie River delta, where OC_{petro} accounts for ~10–30% of total particulate organic carbon³⁴. In general, the OC_{petro} fractions during the last deglaciation were one- to threefold higher than those in the late Holocene (Supplementary Table 1). In a conservative estimate, the TOC MARs during the deglaciation ($-0.38 \text{ g cm}^{-2} \text{ kyr}^{-1}$) were ~six times higher than those in the late Holocene ($-0.06 \text{ g cm}^{-2} \text{ kyr}^{-1}$) (see more information in Supplementary Discussion). We thus conclude that the OC_{petro} MARs were 6–18 (or 12 ± 6) times higher during the last deglaciation.

The climate impact of OC_{petro} exhumation during the last deglaciation is currently uncertain and depends on the fate of remobilized carbon. Through a simple pathway, the remobilized OC_{petro} escaped remineralization and translocated from sedimentary rocks to oceanic storage which has negligible impacts on atmospheric CO_2 levels, while when through an oxidation pathway the remobilized OC_{petro} was reintroduced into the carbon cycle which may affect atmospheric carbon chemistry. Emerging evidence couples OC_{petro} oxidation flux with rock erosion rate¹³, and particularly, the recent study observed higher CO_2 emissions in glaciated areas than in unglaciated areas¹⁵. The evidence provides us with the basis to explore an alternative scenario of large OC_{petro} oxidation during the last deglaciation. Reconstructing oxidation of exhumed OC_{petro} for past time periods is not possible from direct observations, but insights might be gained by studying sedimentary records. When postulating that our core record is representative of the process of petrogenic carbon mobilization in response to the deglaciation of North America, the record provides us with the opportunity to explore the effect enhanced rock erosion might have had on atmospheric CO_2 .

Modern observations suggest that ~10–90% of the exhumed OC_{petro} are oxidized, percentages varying in different regions, whereas OC_{petro} buried in river/marine sediments is unoxidized and may be chemically and physically resilient¹³. Regarding the increased OC_{petro} MARs as a consequence of enhanced rock erosion and assuming a constant burial efficiency, the OC_{petro} oxidized should always keep pace with that accumulated in marine sediments. Therefore, the increase in OC_{petro} MARs indicates an increase in OC_{petro} oxidation flux by 6–18 (12 ± 6) times during the last deglaciation when compared to the modern oxidation flux. In the Mackenzie River basin, the modern OC_{petro} oxidation fluxes are estimated to be $-0.45 \pm 0.19 \text{ tC km}^{-2} \text{ yr}^{-1}$ for the Mackenzie River and a mean value of $0.89 \pm 0.32 \text{ tC km}^{-2} \text{ yr}^{-1}$ for its main tributaries ($0.94^{+0.41/-0.26}$, $0.78^{+0.35/-0.21}$, and $1.01^{+0.42/-0.25} \text{ tC km}^{-2} \text{ yr}^{-1}$ for the Peel, Arctic Red, and Liard River, respectively)⁴³. The oxidation flux along the Mackenzie River is moderate in comparison to its tributaries. This can be explained by the fact that only 54% of the entire basin is on shales while all the tributaries drain through the shales-dominated mountain regions⁴⁴. Therefore, the mean value ($0.89 \pm 0.32 \text{ tC km}^{-2} \text{ yr}^{-1}$) from the main tributaries is taken to represent the OC_{petro} oxidation flux in shales regions, which is estimated to be $11 \pm 7 \text{ tC km}^{-2} \text{ yr}^{-1}$ during the last deglaciation.

One should keep in mind that physical erosion was not the only factor responsible for the increases in OC_{petro} MAR. Organic carbon burial efficiency increases with higher sedimentation rates^{45,46}. On a larger spatial scale, global TOC MARs during the LGM were $147 \pm 18\%$ relative to the Holocene and then gradually decreased to the Holocene level⁴⁷. This may indicate more efficient OC transfer from the sea surface to the seafloor and better preservation in marine sediment during the last deglaciation. In the study area, the meltwater-induced high discharge and shorter pathways from glaciers to the ocean may have further shortened the transport time, reducing OC oxidation during transport, and thus increased the OC burial efficiency in marine sediments. Besides, lower sea-level and closer distance of the study site to the coast may have caused higher OC_{petro} MARs during the last deglaciation. While in opposite to the extensive shelves in the Laptev Sea or the East Siberian Sea, the offshore distance may change less in the Beaufort Sea due to the narrow shelf. Because the OC_{petro} burial

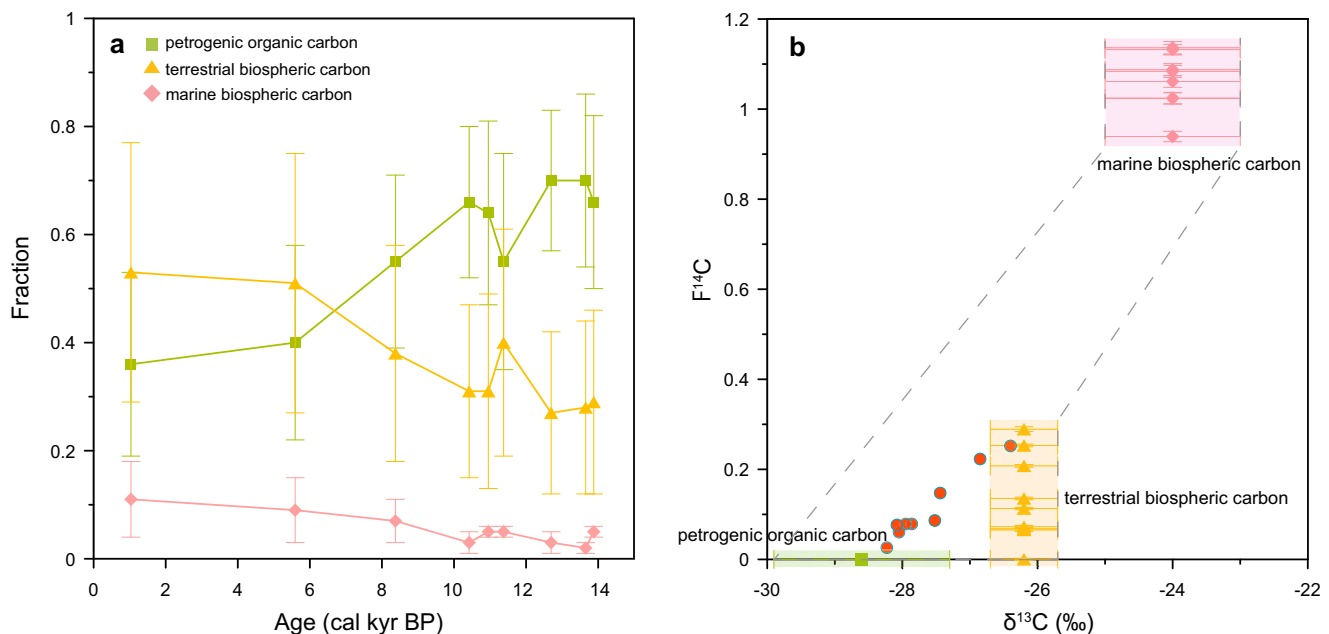


Fig. 4 | Dual-isotope mixing model and source apportionments. **a** OC fractions from different carbon sources. Error bars represent standard deviation; **b** $\delta^{13}\text{C}$ and $F^{14}\text{C}$ values of measured samples (red dots) and of endmembers for marine

biospheric carbon (pink diamonds), terrestrial biospheric carbon (yellow triangles), and petrogenic organic carbon (green squares) used in a dual-isotope mixing model. Error bars represent standard deviation.

efficiency might have increased via multiple processes during the last deglaciation, the estimated OC_{petro} oxidation flux must therefore be regarded as an upper limit.

On the other hand, there are reasons that we would argue to expect even larger oxidation fluxes than we predicted. Glacial processes appear to enhance OC_{petro} oxidation flux even at the same rate of physical erosion¹⁵. Besides, not all of the exhumed OC_{petro} was transported to the ocean, and much of the glacially eroded material may have been deposited on land (e.g., moraines) or trapped in an intermediate pool of glacial lakes⁴⁸. The enhanced OC_{petro} MARs in marine records thus only reflect part of the exhumed OC_{petro} . These characteristics in the glacial watersheds imply that extrapolating oxidation flux from an unglaciated modern environment to a glaciated paleo scenario may cause an underestimate.

Outcropping shales that were exposed by glacial retreat after long-term isolation may have released additional CO_2 into the atmosphere. Estimating OC_{petro} oxidation flux in such regions allows for a quantitative estimate of carbon release. The carbon yield (J_{carbon}) from OC_{petro} oxidation can be estimated based on the exposed area (A_{exposure}), oxidative weathering fluxes ($F_{\text{oxidation}}$), and the exposure time (T_{exposure}) using the equation:

$$J_{\text{carbon}} = A_{\text{exposure}} \times F_{\text{oxidation}} \times T_{\text{exposure}} \quad (1)$$

The A_{exposure} is defined as freshly exposed areas with outcropping shales during the ice-sheet retreat. The area changes through time with regard to ice-sheet retreat, we, therefore, calculate A_{exposure} based on shales distribution and the changes in ice-sheet extent^{44,49} in North America (Fig. 5a; 180°W–75°W, 45°N–90°N). Because we assume that freshly exposed shales have higher oxidation flux and the flux decreases over time (discussed below), the A_{exposure} is calculated in steps of 500 years to indicate the freshly exposed shales area in different time periods. The $F_{\text{oxidation}}$ is defined as OC_{petro} oxidation flux for shales regions. Here we take $F_{\text{oxidation}}$ from the main tributaries of the Mackenzie River and assume it is applicable to entire North America. In the Mackenzie River basin, $F_{\text{oxidation}}$ is known to be $0.89 \pm 0.32 \text{ tC km}^{-2} \text{ yr}^{-1}$ in the contemporary system⁴³ and is estimated (based on the increased OC_{petro} MARs that reflect strongly increased erosion) to be $11 \pm 7 \text{ tC km}^{-2} \text{ yr}^{-1}$ during the last deglaciation. From the last deglaciation towards the present, the large decrease in $F_{\text{oxidation}}$ may reflect processes such as soil formation and vegetation development, which reduce $F_{\text{oxidation}}$ with increasing exposure time. To include such processes in the calculation, we assume that $F_{\text{oxidation}}$ decreases with increasing substrate age in a similar manner as in silicate weathering (i.e., $F_{\text{oxidation}} = F_0 \times t^{-0.71}$)^{50,51}. F_0 is the oxidation flux of freshly exposed substrate (10-year-old), and $F_{\text{oxidation}}$ denotes the oxidation flux of the substrate at age t . Calculation of F_0 requires a given $F_{\text{oxidation}}$ with a known substrate age t . Since Horan et al.⁴³ have estimated the modern oxidation flux ($0.89 \pm 0.32 \text{ tC km}^{-2} \text{ yr}^{-1}$) for the shales-dominated region and the region is known to have been exposed between 15 and 10 cal. kyr BP¹⁹, we thus assume for 10^4 years old substrates (t) an oxidation rate of $1 \text{ tC km}^{-2} \text{ yr}^{-1}$ ($F_{\text{oxidation}}$) and obtain for newly exposed shales a rate of $21 \text{ tC km}^{-2} \text{ yr}^{-1}$ (F_0). Uncertainty bands are added to this approach by assuming that the modern $F_{\text{oxidation}}$ ($-1 \text{ tC km}^{-2} \text{ yr}^{-1}$) is alternatively valid for substrate ages of 5 kyrs or 15 kyrs (Fig. 5b). Although the long-term behavior of $F_{\text{oxidation}}$ is implemented based on the modern oxidation flux, the oxidation fluxes during the last deglaciation that we derived from the data obtained on our sediment core ($11 \pm 7 \text{ tC km}^{-2} \text{ yr}^{-1}$) fall well within the range and correspond to a substrate age of <100 to 2000 years (indicated in Fig. 5b), to some degree supporting our assumption. Due to the variable $F_{\text{oxidation}}$ over time, carbon release (J_{carbon}) is calculated in steps of 100 years for entire North America and has been integrated over all time steps. The annual carbon release for entire North America is shown in Fig. 5c, with a cumulative release of $84 \pm 30 \text{ PgC}$.

Besides the exhumation of OC_{petro} during the last deglaciation, the events of increased TOC MARs also provide evidence for coastal erosion of permafrost that occurred in well-defined pulses. Because inland permafrost formation was restricted in the Mackenzie River basin, the maxima in accumulation occurring in the PreBoreal (MWP1b) and at or around MWP 1a were most likely attributed to the erosion of non-glaciated coastal permafrost (e.g., derived from Yukon coast), OC-rich deposits from the eastern coast, and residual permafrost/soil deposited in coastal regions. Within dating uncertainties, these two events were broadly coeval with those found in other records across the North Pacific and the Arctic Ocean^{17,23,24,26}. Therefore, our records confirm that coastal erosion induced by rapid sea-level rise was a major process of aged permafrost carbon release in (sub-)Arctic coasts and shelves.

Remobilized permafrost carbon has been proposed to be highly bioavailable. A recent study mimics coastal permafrost erosion by incubating permafrost with and without seawater for the duration of one Arctic open-water season⁵². The authors demonstrate that substantial amounts of OC are quickly re-mineralized in all incubations, and the CO_2 production is even higher when seawater is added, indicating potentially substantial CO_2 emissions from erosion of permafrost onshore and within the nearshore waters. Estimates from Herschel Basin, a shelf basin in the Beaufort Sea, suggest that only ~40% of the eroded permafrost carbon from adjacent Herschel Island is buried locally in the basin³², where it may, however, be further degraded. Another study based on OC concentrations of thawed samples from eroded bluffs estimates that ~66% of the OC contained in Yedoma deposits is released as CO_2 in one thawing season, prior to reaching a water body downslope⁵³. Accordingly, the eroded permafrost carbon may have contributed to rapid deglacial CO_2 rises.

The two processes of carbon release, i.e., exhumation of OC_{petro} and destabilization of coastal permafrost deposits, are both related to ice-sheet retreat. Ice-sheet retreat directly led to erosion, exposure, and oxidation of OC_{petro} which released, depending on assumed substrate age, $84 \pm 30 \text{ Pg}$ of carbon. At the same time, the reduction in ice volume resulted in sea-level rise leading to coastal erosion/shelf flooding of permafrost from the Arctic shelves, which is estimated to release 85 Pg of carbon²⁴. We applied the most recent version of the global carbon cycle model BICYCLE³⁰ in order to assess the impacts of ice-sheet retreat via the combined processes mentioned above on atmospheric CO_2 and $\Delta^{14}C$. The carbon release rate from OC_{petro} oxidation is shown in Fig. 5c. Since our sedimentary records confirm coastal erosion during the rapid sea-level rise as a major process to release permafrost carbon in pulses, the carbon release rate from coastal permafrost follows the simulation in Winterfeld et al.²⁴, i.e., the release of 10 kyr-old permafrost carbon is restricted to a time window of 200 years for three pulses: 170 TgC yr^{-1} (or 34 PgC) at 11.5 and 14.6 cal. kyr BP each and 85 TgC yr^{-1} (or 17 PgC) at 16.5 cal. kyr BP. All carbon is released as CO_2 and directly enters the atmosphere in the model.

The results show three simulated peaks which are solely caused by the pulses of permafrost carbon release. These events include a first CO_2 peak of 6 ppm at 16.5 cal. kyr BP and two more CO_2 peaks of -12 ppm at 14.6 and 11.5 cal. kyr BP (Fig. 5d). These permafrost carbon release pulses lead in the model to a decrease in $\Delta^{14}C$ of -10 permil at 16.5 cal. kyr BP and of -13–15 permil at 14.6 cal. kyr BP and 11.5 cal. kyr BP (Fig. 5e). The contribution of OC_{petro} from North American shales adds a long-term rise of 4 ± 1 ppm to atmospheric CO_2 and of -4 ± 1 permil to atmospheric $\Delta^{14}C$. The simulated long-term effects over the last 20 kyrs when combining both processes are an increase in atmospheric CO_2 by 12 ppm and a decrease in atmospheric $\Delta^{14}C$ by 12 permil (Figs. 5d, e), explaining 13% and 3%, respectively, of the reconstructed changes in both variables.

Our attempt at a quantitative estimate of OC_{petro} release, combined with coastal permafrost carbon release, demonstrates positive

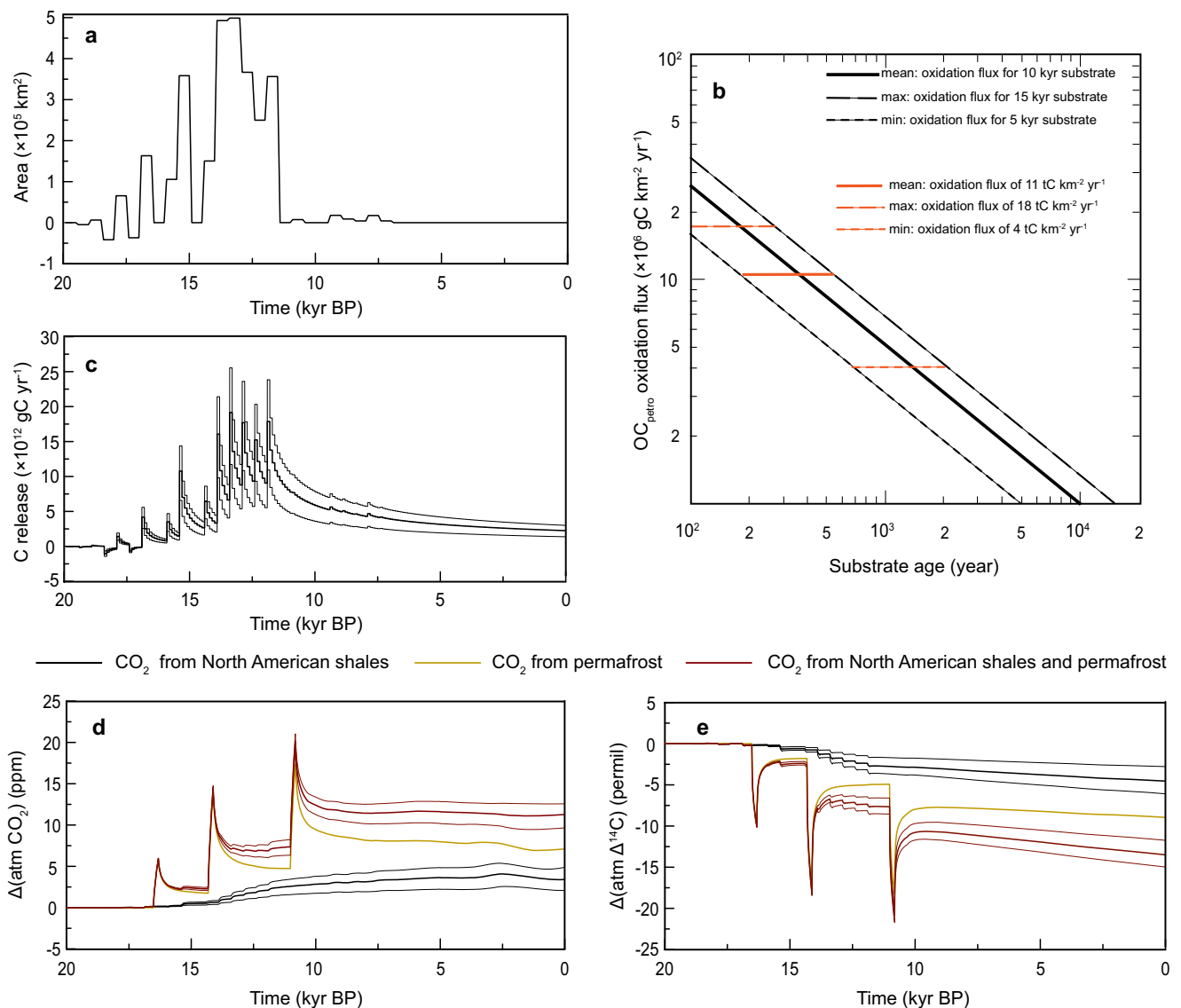


Fig. 5 | Carbon release from OC_{petro} oxidation and simulated impacts on atmospheric CO_2 . **a** areas of the ice-sheet retreat on shales calculated in steps of 500 years, based on the shales distribution and ice-sheet extent in North America^{44,49}; **b** assumed long-term OC_{petro} (petrogenic organic carbon) oxidation fluxes ($F_{\text{oxidation}}$) with substrate age (t) in North America, following the equation $F_{\text{oxidation}} = F_0 \times t^{-0.71}$. The black solid line demonstrates a scenario that the modern $F_{\text{oxidation}} = 1 \text{ tC km}^{-2} \text{ yr}^{-1}$ is valid for shales of a substrate age of 10 kyrs, and the black

dashed lines indicate scenarios that the modern $F_{\text{oxidation}} = 1 \text{ tC km}^{-2} \text{ yr}^{-1}$ is valid for shales of a substrate age of 5 and 15 kyrs, respectively. Red lines mark the estimated past OC_{petro} oxidation fluxes derived from the data of core ARA04C/37; **c** carbon release from OC_{petro} oxidation, short-term peaks are attributed to the J_{carbon} calculated in steps of 100 years for every 500-year exposed areas; simulated anomalies in **d** atmospheric CO_2 levels and in **e** atmospheric $\Delta^{14}\text{C}$ using the global carbon cycle model BICYCLE³⁰.

feedback of the ice-sheet retreat that may partially explain the deglacial atmospheric CO_2 rise. Notably, OC_{petro} release from North America is only one of the processes that are coupled with ice-sheet retreat, while the local net CO_2 budget must involve multiple other processes. Although sulfide weathering does not release CO_2 , its product, sulfuric acid may increase carbonate solubility and thus boost CO_2 emissions from carbonate weathering, which is described as a supply-limited process^{13,54}. In contrast, silicate weathering is known to be a process of long-term drawdown of atmospheric CO_2 , and its associated carbon flux is sensitive to climate change and depends weakly on the erosion rate¹³. The burial of $\text{OC}_{\text{terr-bio}}$ by erosion is proven to be an important geological CO_2 sink³⁴. By considering CO_2 emissions from oxidative weathering as well as CO_2 drawdown by $\text{OC}_{\text{terr-bio}}$ burial and silicate weathering, Horan et al.⁴³ have estimated for the modern Mackenzie River catchment a net transfer of CO_2 from the atmosphere to the lithosphere, with a flux of $-1 \text{ tC km}^{-2} \text{ yr}^{-1}$. Using modern unglaciated

situations as analogs, the authors further postulate that the Mackenzie River catchment was a net CO_2 source during the LGM due to the reasons that (1) glacial erosion of sedimentary rocks may have strengthened oxidative weathering, (2) lower temperature may have weakened CO_2 drawdown by silicate weathering, and (3) limited vegetation and soils may have resulted in lower $\text{OC}_{\text{terr-bio}}$ stock in the landscape and weakened CO_2 drawdown by $\text{OC}_{\text{terr-bio}}$ burial. Our study presents direct evidence of substantial OC_{petro} remobilization that may support the strengthened OC_{petro} oxidative weathering during the last deglaciation. Besides, the very old $\text{OC}_{\text{terr-bio}}$ in our sediment archive most likely reflects limited vegetation in the glaciated environment (Fig. 3e), implying less fresh $\text{OC}_{\text{terr-bio}}$ burial. From a perspective of OC dynamics, our records support the Mackenzie River catchment as a net carbon source during the last deglaciation. However, the magnitude of net CO_2 release from this region requires a comprehensive understanding of how ice-sheet retreat is involved in both inorganic and

organic processes. Vegetation development and permafrost soil formation, in combination with weakening weathering processes, may have played a key role in transforming the region from a carbon source to a carbon sink during the glacial-interglacial transition.

Overall, the study provides evidence for enhanced OC_{petro} exhumation and rapid coastal erosion events during the last deglaciation. Under the assumption of extensive OC_{petro} oxidation during the glacial retreat, carbon release from the two processes contributes to the deglacial rise in atmospheric CO₂. The ice-sheet retreat has played a crucial role in mobilizing these aged/ancient terrestrial OC. These findings underscore the view that ice sheets may play an active role in the global carbon cycle during deglaciation. More work is needed to investigate carbon dynamics related to ice-sheet retreat, including oxidative weathering, silicate weathering, and biospheric carbon burial. Besides, it is essential to investigate carbon sources and carbon characteristics in other glaciated regions and to explore their roles in the deglacial carbon cycle.

Methods

Core location and sediment chronology

Gravity core ARA04C/37 was collected during the Araon Cruise ARA04C⁵⁵ at the Beaufort Sea continental slope, with a recovery of 595 cm (Fig. 1; 70°38.0212'N, 139°22.0749'W; 1173 m). The age-depth model of core ARA04C/37 has been established by Wu et al.²⁸ based on AMS¹⁴C dating on calcareous foraminifera and, in the uppermost centimeters, excess ²¹⁰Pb. This study updates the age-depth model by dating planktic foraminifera from the B/A interval, adding two new AMS¹⁴C dates to the age-depth model (Supplementary Table 2). The base of core ARA04C/37 could not be dated due to a lack of planktic foraminifera. Therefore, the age model from Wu et al.²⁸, which is based on the correlation of magnetic susceptibility data between ARA04C/37 and nearby core JPC15 (Fig. 1), is adopted without further modification for the depths below 530 cm. Because our study focuses partly on the centennial rapid events, we used the Marine13 calibration curve to keep consistency with other published records^{17,24}.

Core JPC15 was obtained at the continental slope east of Mackenzie River (Fig. 1; 71°06.222'N, 135°08.129'W; 690 m). Samples from the B/A interval of core JPC15 were analyzed for this study. For more information and chronology of sediment core JPC15, please refer to Keigwin et al.²⁹.

Rock-Eval pyrolysis

Rock-Eval pyrolysis was performed on bulk sediment samples according to Espitalie et al.³⁶. Hydrogen and oxygen contents of the samples, measured as hydrocarbon-type compound and carbon dioxide yields respectively, were normalized to organic carbon and displayed as hydrogen index (mgHC/gC) and oxygen index (mgCO₂/gC). In a van Krevelen-type diagram, a classification illustrating carbon types is possible³⁷. Furthermore, the temperature at which pyrolysis yields the maximum of hydrocarbons (T_{max}) is used as an indicator of the thermal maturity of the kerogen. Immature organic matter usually has T_{max} values of <435 °C.

Biomarker analyses and thermal maturity indicators

Freeze-dried sediments (~5 g) were extracted with DCM:MeOH (2:1, v/v), and an internal standard (Squalane, 2.4 µg/sample) was added prior to analytical treatment. Total lipid extracts were concentrated and separated into a hydrocarbon fraction (containing *n*-alkanes and hopanes) and an alcohol fraction via open column chromatography with silica gel (6 mm i.d.*4.5 cm). Hydrocarbon fractions were eluted with 5 ml *n*-hexane, followed by alcohol fraction elution with 9 ml ethyl acetate:*n*-hexane (1:4, v/v).

The *n*-alkanes were analyzed using a gas chromatograph (GC, Agilent 7890 A) coupled to a flame ionization detector (GC-FID). Homohopane isomers were analyzed with an Agilent 6850 gas

chromatograph (GC) coupled to an Agilent 5975 C VL MSD quadrupole mass spectrometer operating in electron impact ionization (70 eV) and full-scan (*m/z* 50–600) mode.

The *n*-alkanes were identified with external standards, and the carbon preference index of *n*-alkanes (CPI_{alk}) was calculated as follows (Eq. 2):

$$\text{CPI}_{\text{alk}} = \frac{1}{2} \times \left(\frac{\text{C}_{23} + \text{C}_{25} + \text{C}_{27} + \text{C}_{29} + \text{C}_{31}}{\text{C}_{22} + \text{C}_{24} + \text{C}_{26} + \text{C}_{28} + \text{C}_{30}} + \frac{\text{C}_{23} + \text{C}_{25} + \text{C}_{27} + \text{C}_{29} + \text{C}_{31}}{\text{C}_{24} + \text{C}_{26} + \text{C}_{28} + \text{C}_{30} + \text{C}_{32}} \right) \quad (2)$$

CPI_{alk} > 3 is indicative for significant contributions of fresh OC from immature deposits, whereas CPI_{alk} close to 1 is indicative for a dominance of thermally mature OC (ref. 17 and references therein). Because CPI_{alk} may also vary with OC degradation state³⁸, a combination with the relative abundances of homohopane isomers (fββ) can further indicate contributions from thermally mature OC.

Homohopane isomers (C₃₁) were identified by relative retention times and mass spectra¹⁷. The relative abundance of the “biogenic isomer” 17β,21β(H) 22 R (C₃₁ββR) to the “diagenetic isomers” 17β,21α(H) 22 R (C₃₁βαR), 17β,21α(H) 22 S (C₃₁βαS), 17α,21β(H) 22 R (C₃₁αβR), and 17α,21β(H) 22 S (C₃₁αβS) is described as Eq. 3¹⁷:

$$f\beta\beta = \frac{\text{C}_{31}\beta\beta\text{R}}{\text{C}_{31}\beta\beta\text{R} + \text{C}_{31}\alpha\beta\text{S} + \text{C}_{31}\alpha\beta\text{R} + \text{C}_{31}\beta\alpha\text{S} + \text{C}_{31}\beta\alpha\text{R}} \quad (3)$$

Values of 1 indicate the absence of “diagenetic isomers”, whereas values of 0 indicate the absence of “biogenic isomer”.

Radiocarbon analyses of bulk OC and HMW-FAs

Radiocarbon dating was performed following methods described in Mollenhauer et al.⁵⁹. Briefly, according to the respective TOC contents, sediment samples containing ~1 mg OC were weighed into silver capsules and were acidified with 6 N hydrochloric acid (HCl) to completely remove the inorganic carbon. Acid evaporation was conducted on a hot plate at 60 °C, and the dried samples were then stored in an oven (60 °C) until the analysis. Samples including the silver capsules were packed into tin capsules and combusted individually via an Elemental vario ISOTOPE EA (Elemental Analyzer). Oxidized carbon (CO₂) was directly graphitized by the Ionplus AGE3 system (Automated Graphitization System)⁶⁰. Radiocarbon contents of samples were analyzed using the Ionplus MICADAS dating system^{61,62}.

For compound-specific (HMW-FAs) radiocarbon dating, sediment samples (~50–70 g) were extracted with DCM:MeOH (9:1, v/v) using a Soxhlet for over 48 h. The total extracts were hydrolyzed with potassium hydroxide (KOH, 0.1 M) in MeOH:H₂O (9:1, v/v) at 80 °C for 2 h. The neutral lipids were extracted with *n*-hexane, and the *n*-alkanoic acids were then extracted with DCM after adjusting the pH to a value of around 2 by the addition of 37% HCl. The extracted *n*-alkanoic acids were methylated with 37% HCl and MeOH with a known ¹⁴C-signature in a nitrogen atmosphere at 80 °C for over 12 h. The fatty acid methyl esters (FAMES) were extracted with *n*-hexane and subsequently separated from polar compounds by silica gel chromatography.

FAMES with chain lengths >C₂₄ were purified by preparative capillary gas chromatography (PC-GC) using an Agilent 6890 N GC equipped with a Gerstel Cooled Injection System (GIS) and connected to a Gerstel preparative fraction collector⁶³. The GC was equipped with a Restek Rxi-XLB fused silica capillary column (30 m, 0.53 mm i.d., 0.5-µm film thickness). All samples were injected stepwise with 5 µL per injection. Afterwards, the purified individual FAMES were transferred into tin capsules and packed. Samples were combusted via the Elemental vario ISOTOPE EA (Elemental Analyzer), and the isotopic ratios (¹⁴C/¹²C) of produced CO₂ were determined via the directly connected AMS, the MICADAS system, which is equipped with a gas-ion source.

Radiocarbon contents of the samples were analyzed along with reference standards (oxalic acid II; NIST 4990c) and blanks (phthalic anhydride; Sigma-Aldrich 320064) and in-house reference sediments. Blank correction and standard normalization were performed via the BATS software⁶⁴. All results are reported as fraction modern carbon ($F^{14}\text{C}$).

Blank assessment and corrections

Compound-specific samples analyzed for radiocarbon are sensitive to contamination during processing (procedure blank), for example, the carbon introduced via column bleed and carry-over as well as from the tin capsules. Blank correction of compound-specific samples requires careful determination of $F^{14}\text{C}$ of the blank and the size of blank. For this purpose, radiocarbon analyses of in-house reference samples from ^{14}C -free Eocene Messel Shale ($F^{14}\text{C}_{\text{OC}} = 0$) and modern apple peel ($F^{14}\text{C}_{\text{OC}} = 1.029 \pm 0.001$) processed in the same way as the compound-specific samples were conducted to determine the $F^{14}\text{C}$ and mass of blank, following the method of Sun et al.⁶⁵. All radiocarbon data were corrected for the procedural blank and, to remove the contribution of the methyl group added during the derivatization process, a methyl correction was further performed through isotopic mass balance. Uncertainties were fully propagated.

Pre-depositional ages of OC

The pre-depositional age of OC can be derived from the initial radiocarbon content ($\Delta^{14}\text{C}_{\text{initial}}$; radiocarbon content prior to the OC deposition to marine sediment), which has been calculated based on the following equation:⁶⁶

$$\Delta^{14}\text{C}_{\text{initial}} = (F^{14}\text{C} e^{\lambda t} - 1) \times 1000\text{‰} \quad (4)$$

$F^{14}\text{C}$ is the measured fraction modern carbon, and for compound-specific samples, the blank- and methanol-corrected $F^{14}\text{C}$ values are used. λ is the decay constant of radiocarbon, and t is the time since deposition (according to the core chronology).

The radiocarbon content of the past atmosphere differed from the modern atmosphere, and thus the atmospheric radiocarbon content at the time of deposition ($\Delta^{14}\text{C}_{\text{atm}}$) was taken from the atmospheric $\Delta^{14}\text{C}$ record of IntCal13 (for consistency, as Marine13 was used for the age model)⁶⁷. The apparent conventional ^{14}C age (pre-depositional age) thus has been calculated by the following equation:⁶⁶

$$\text{pre-depositional age} = -8033 \times \ln \left[\frac{1 + \Delta^{14}\text{C}_{\text{initial}}/1000}{1 + (\Delta^{14}\text{C}_{\text{atm}}/1000)} \right] \quad (5)$$

Carbon cycle modeling

We use the most recent version of the global carbon cycle model BICYCLE³⁰ to simulate the impact of the released carbon on atmospheric CO_2 and $\Delta^{14}\text{C}$. This version, called BICYCLE-SE, includes solid Earth processes (volcanic CO_2 outgassing, continental weathering, shallow water carbon sink in coral reefs) and a process-based sediment model, which calculates as function of the depth-dependent carbonate ion concentrations the accumulation or dissolution of CaCO_3 in the deep ocean sediments. The core of the model still consists of a 10-box ocean, a 1-box atmosphere, and a 7-box terrestrial biosphere. We calculate the contribution from OC_{petro} released from a retreating LIS on shales (Fig. 5c) and permafrost²⁴, by additional carbon fluxes to a control run, which is based on the scenario SE in Köhler and Munhoven³⁰ with the exception of a passive (constant) terrestrial carbon pool. This has been chosen to make simulation results comparable to Winterfeld et al.²⁴, in which a similar setup, but using an older model version, has been applied. The ^{14}C production rate is kept constant at 25% higher than preindustrial levels in order to obtain at LGM an atmospheric $\Delta^{14}\text{C}$ of ~ 400 permil, comparable to reconstructions.

Simulations are initialized with interglacial conditions, and the state variables of the sediment are taken after an 800 kyr-long spinup, and started at 210 cal. kyr BP to give the model enough time to run into a reasonable state which is largely independent from initial conditions and spinup.

While we use three different versions of the fluxes for OC_{petro} depending on the assumed substrate age (5, 10, 15 kyrs), we use only one version of the permafrost-based carbon release related to coastal erosion. Here, 17, 34, and 34 Pg of 10 kyr-old carbon are released in three 200-year-long pulses starting at 16.5, 14.6, and 11.5 cal. kyr BP²⁴. The carbon released from both processes is entering the model as ingoing CO_2 fluxes to the atmosphere. The time-dependent forcing—the changes in climatic boundary conditions (e.g., temperature, sea-level, sea ice, ocean circulation, iron input to the marine biology)—is otherwise identical to what is described in Köhler and Munhoven³⁰.

Data availability

The data generated in this study have been deposited in the PANGAEA repository (<https://doi.org/10.1594/PANGAEA.939847>)⁶⁸. Source data are provided with this paper.

References

- Marcott, S. A. et al. Centennial-scale changes in the global carbon cycle during the last deglaciation. *Nature* **514**, 616–619 (2014).
- Monnin, E. et al. Atmospheric CO_2 concentrations over the last glacial termination. *Science* **291**, 112–114 (2001).
- Reimer, P. J. et al. The IntCal20 Northern Hemisphere radiocarbon age calibration curve (0–55 cal kBP). *Radiocarbon* **62**, 725–757 (2020).
- Anderson, B. E. & Burckle, L. H. Wind-driven upwelling in the southern ocean and the deglacial rise in atmospheric CO_2 . *Science* **323**, 1443–1448 (2009).
- Köhler, P., Fischer, H., Munhoven, G. & Zeebe, R. E. Quantitative interpretation of atmospheric carbon records over the last glacial termination. *Glob. Biogeochem. Cycles* **19**, 1–24 (2005).
- Bauska, T. K. et al. Carbon isotopes characterize rapid changes in atmospheric carbon dioxide during the last deglaciation. *Proc. Natl Acad. Sci.* **113**, 3465–3470 (2016).
- Rae, J. W. B. et al. CO_2 storage and release in the deep Southern Ocean on millennial to centennial timescales. *Nature* **562**, 569–573 (2018).
- Wadham, J. L. et al. Ice sheets matter for the global carbon cycle. *Nat. Commun.* **10**, 1–17 (2019).
- Vinšová, P. et al. The biogeochemical legacy of arctic subglacial sediments exposed by glacier retreat. *Glob. Biogeochem. Cycles* **36**, e2021GB007126 (2022).
- Blattmann, T. M. Ideas and perspectives: emerging contours of a dynamic exogenous kerogen cycle. *Biogeosciences* **19**, 359–373 (2022).
- Chang, S. & Berner, R. A. Coal weathering and the geochemical carbon cycle. *Geochim. Cosmochim. Acta* **63**, 3301–3310 (1999).
- Petsch, S. T., Eglinton, T. I. & Edwards, K. J. C-dead living biomass: evidence for microbial assimilation of ancient organic carbon during shale weathering. *Science* **292**, 1127–1131 (2001).
- Hilton, R. G. & West, A. J. Mountains, erosion and the carbon cycle. *Nat. Rev. Earth Environ.* **1**, 284–299 (2020).
- Hilton, R. G., Gaillardet, J. Ö., Calmels, D. & Birck, J. L. Geological respiration of a mountain belt revealed by the trace element rhenium. *Earth Planet. Sci. Lett.* **403**, 27–36 (2014).
- Horan, K. et al. Mountain glaciation drives rapid oxidation of rock-bound organic carbon. *Sci. Adv.* **3**, e1701107 (2017).
- Cui, X., Bianchi, T. S., Jaeger, J. M. & Smith, R. W. Biospheric and petrogenic organic carbon flux along southeast Alaska. *Earth Planet. Sci. Lett.* **452**, 238–246 (2016).

17. Meyer, V. D. et al. Permafrost-carbon mobilization in Beringia caused by deglacial meltwater runoff, sea-level rise and warming. *Environ. Res. Lett.* **14**, 085003 (2019).
18. Dyke, A. S. An outline of North American deglaciation with emphasis on central and northern Canada. *Dev. Quat. Sci.* **2**, 373–424 (2004).
19. Dalton, A. S. et al. An updated radiocarbon-based ice margin chronology for the last deglaciation of the North American Ice sheet complex. *Quat. Sci. Rev.* **234**, 106223 (2020).
20. Copard, Y., Amiotte-Suchet, P. & Di-Giovanni, C. Storage and release of fossil organic carbon related to weathering of sedimentary rocks. *Earth Planet. Sci. Lett.* **258**, 345–357 (2007).
21. Campeau, A., Soerensen, A., Martma, T., Åkerblom, S. & Zdanowicz, C. Controls on the 14 C-content of dissolved and particulate organic carbon mobilized across the Mackenzie River basin, Canada. *Glob. Biogeochem. Cycles* **34**, e2020GB006671 (2020).
22. Köhler, P., Knorr, G. & Bard, E. Permafrost thawing as a possible source of abrupt carbon release at the onset of the Bølling/Allerød. *Nat. Commun.* **5**, 5520 (2014).
23. Martens, J. et al. Remobilization of dormant carbon from Siberian-Arctic permafrost during three past warming events. *Sci. Adv.* **6**, eabb6546 (2020).
24. Winterfeld, M. et al. Deglacial mobilization of pre-aged terrestrial carbon from degrading permafrost. *Nat. Commun.* **9**, 3666 (2018).
25. Kesikitalo, K. et al. Sources and characteristics of terrestrial carbon in Holocene-scale sediments of the East Siberian Sea. *Clim. Past* **13**, 1213–1226 (2017).
26. Martens, J. et al. Remobilization of old permafrost carbon to Chukchi sea sediments during the end of the last deglaciation. *Glob. Biogeochem. Cycles* **33**, 2–14 (2019).
27. Tesi, T. et al. Massive remobilization of permafrost carbon during post-glacial warming. *Nat. Commun.* **7**, 13653 (2016).
28. Wu, J. et al. Deglacial to Holocene variability in surface water characteristics and major floods in the Beaufort Sea. *Commun. Earth Environ.* **1**, 27 (2020).
29. Keigwin, L. D. et al. Deglacial floods in the Beaufort Sea preceded Younger Dryas cooling. *Nat. Geosci.* **11**, 599–604 (2018).
30. Köhler, P. & Munhoven, G. Late pleistocene carbon cycle revisited by considering solid earth processes. *Paleoceanogr. Paleoclimatol.* **35**, e2020PA004020 (2020).
31. Holmes, R. M. et al. A circumpolar perspective on fluvial sediment flux to the Arctic ocean. *Glob. Biogeochem. Cycles* **16**, 1098 (2002).
32. Grotheer, H. et al. Burial and origin of permafrost derived carbon in the nearshore zone of the southern Canadian Beaufort Sea. *Geophys. Res. Lett.* **47**, e2019GL085897 (2020).
33. Goñi, M. A., Yunker, M. B., Macdonald, R. W. & Eglinton, T. I. The supply and preservation of ancient and modern components of organic carbon in the Canadian Beaufort Shelf of the Arctic Ocean. *Mar. Chem.* **93**, 53–73 (2005).
34. Hilton, R. G. et al. Erosion of organic carbon in the Arctic as a geological carbon dioxide sink. *Nature* **524**, 84–87 (2015).
35. Fisher, T. G., Waterson, N., Lowell, T. V. & Hajdas, I. Deglaciation ages and meltwater routing in the Fort McMurray region, north-eastern Alberta and northwestern Saskatchewan, Canada. *Quat. Sci. Rev.* **28**, 1608–1624 (2009).
36. Murton, J. B., Bateman, M. D., Dallimore, S. R., Teller, J. T. & Yang, Z. Identification of Younger Dryas outburst flood path from Lake Agassiz to the Arctic Ocean. *Nature* **464**, 740–743 (2010).
37. Eglinton, T. I. et al. Climate control on terrestrial biospheric carbon turnover. *Proc. Natl Acad. Sci.* **118**, e2011585118 (2021).
38. Kusch, S. et al. Controls on the age of plant waxes in marine sediments – a global synthesis. *Org. Geochem.* **157**, 104259 (2021).
39. Galy, V. & Eglinton, T. Protracted storage of biospheric carbon in the Ganges-Brahmaputra basin. *Nat. Geosci.* **4**, 843–847 (2011).
40. Hein, C. J., Usman, M., Eglinton, T. I., Haghypour, N. & Galy, V. V. Millennial-scale hydroclimate control of tropical soil carbon storage. *Nature* **581**, 63–66 (2020).
41. Tao, S., Eglinton, T. I., Montluçon, D. B., McIntyre, C. & Zhao, M. Pre-aged soil organic carbon as a major component of the Yellow River suspended load: regional significance and global relevance. *Earth Planet. Sci. Lett.* **414**, 77–86 (2015).
42. Brüder, L. et al. Preferential export of permafrost-derived organic matter as retrogressive thaw slumping intensifies. *Environ. Res. Lett.* **10**, 1–16 (2021).
43. Horan, K. et al. Carbon dioxide emissions by rock organic carbon oxidation and the net geochemical carbon budget of the Mackenzie River Basin. *Am. J. Sci.* **319**, 473–499 (2019).
44. Amiotte Suchet, P., Probst, J.-L. & Ludwig, W. Worldwide distribution of continental rock lithology: Implications for the atmospheric/soil CO₂ uptake by continental weathering and alkalinity river transport to the oceans. *Glob. Biogeochem. Cycles* **17**, 1038 (2003).
45. Katsev, S. & Crowe, S. A. Organic carbon burial efficiencies in sediments: the power law of mineralization revisited. *Geology* **43**, 607–610 (2015).
46. David, J. Burdige. Burial of terrestrial organic matter in marine sediments: a re-assessment. *Glob. Planet. Change* **19**, GB4011 (2005).
47. Kandasamy, S. & Nath, B. N. Perspectives on the terrestrial organic matter transport and burial along the land-deep sea continuum: Caveats in our understanding of biogeochemical processes and future needs. *Front. Mar. Sci.* **3**, 259 (2016).
48. Blattmann, T. M., Wessels, M., McIntyre, C. P. & Eglinton, T. I. Petrogenic organic carbon retention in terrestrial basins: a case study from perialpine Lake Constance. *Chem. Geol.* **503**, 52–60 (2019).
49. Peltier, W. R., Argus, D. F. & Drummond, R. Space geodesy constrains ice age terminal deglaciation: the global ICE-6G_C (VM5a) model. *J. Geophys. Res.* **120**, 450–487 (2015).
50. Taylor, A. & Blum, J. D. Relation between soil age and silicate weathering rates determined from the chemical evolution of a glacial chronosequence. *Geology* **23**, 979–982 (1995).
51. Vance, D., Teagle, D. A. H. & Foster, G. L. Variable quaternary chemical weathering fluxes and imbalances in marine geochemical budgets. *Nature* **458**, 493–496 (2009).
52. Tanski, G. et al. Rapid CO₂ release from eroding permafrost in Seawater. *Geophys. Res. Lett.* **46**, 11244–11252 (2019).
53. Vonk, J. E. et al. Activation of old carbon by erosion of coastal and subsea permafrost in Arctic Siberia. *Nature* **489**, 137–140 (2012).
54. Bufe, A. et al. Co-variation of silicate, carbonate and sulfide weathering drives CO₂ release with erosion. *Nat. Geosci.* **14**, 211–216 (2021).
55. Jin, Y. K. *ARA04C Cruise Report: Barrow, US - Beaufort Sea, CAN - Nome, US 6-24 September, 2013.* (2013).
56. Espitalie, J., Madec, M., Tissot, B., Mennig, J. J. & Leplat, P. Source rock characterization method for petroleum exploration. in *Off-shore Technology Conference* 439–443 (1977).
57. Meyers, P. A. & Teranes, J. L. *Sediment organic matter* (Springer, 2002).
58. Brüder, L. et al. Historical records of organic matter supply and degradation status in the East Siberian Sea. *Org. Geochem.* **91**, 16–30 (2016).
59. Mollenhauer, G., Grotheer, H., Gentz, T., Bonk, E. & Hefter, J. Standard operation procedures and performance of the MICADAS radiocarbon laboratory at Alfred Wegener Institute (AWI), Germany. *Nucl. Instrum. Methods Phys. Res., Sect. B: Beam Interact. Mater. At.* **496**, 45–51 (2021).
60. Wacker, L., Němec, M. & Bourquin, J. A revolutionary graphitisation system: Fully automated, compact and simple. *Nucl. Instrum.*

- Methods Phys. Res., Sect. B: Beam Interact. Mater. At.* **268**, 931–934 (2010).
61. Synal, H. A., Stocker, M. & Suter, M. MICADAS: a new compact radiocarbon AMS system. *Nucl. Instrum. Methods Phys. Res., Sect. B: Beam Interact. Mater. At.* **259**, 7–13 (2007).
 62. Wacker, L. et al. Micadas: routine and high-precision radiocarbon dating. *Radiocarbon* **52**, 252–262 (2010).
 63. Kusch, S., Rethemeyer, J., Schefuß, E. & Mollenhauer, G. Controls on the age of vascular plant biomarkers in Black Sea sediments. *Geochim. Cosmochim. Acta* **74**, 7031–7047 (2010).
 64. Wacker, L., Christl, M. & Synal, H. A. Bats: a new tool for AMS data reduction. *Nucl. Instrum. Methods Phys. Res. B* **268**, 976–979 (2010).
 65. Sun, S. et al. ¹⁴C blank assessment in small-scale compound-specific radiocarbon analysis of lipid biomarkers and lignin phenols. *Radiocarbon* **62**, 207–218 (2020).
 66. Schefuß, E. et al. Hydrologic control of carbon cycling and aged carbon discharge in the Congo River basin. *Nat. Geosci.* **9**, 687–690 (2016).
 67. Reimer, P. J. et al. Intcal13 and Marine13 radiocarbon age calibration curves 0–50,000 years Cal Bp. *Radiocarbon* **55**, 1869–1887 (2013).
 68. Wu, J. et al. Biomarker and radiocarbon data of core ARA04C/37 and JPC15 from the Beaufort Sea, Arctic Ocean. *PANGAEA* (2022) <https://doi.org/10.1594/PANGAEA.939847>.
 69. Jakobsson, M. et al. The International Bathymetric Chart of the Arctic Ocean (IBCAO) version 3.0. *Geophys. Res. Lett.* **39**, L12609 (2012).
 70. Köhler, P., Nehrbass-Ahles, C., Schmitt, J., Stocker, T. F. & Fischer, H. A 156 kyr smoothed history of the atmospheric greenhouse gases CO₂, CH₄, and N₂O and their radiative forcing. *Earth Syst. Sci. Data* **9**, 363–387 (2017).
 71. Lambeck, K., Rouby, H., Purcell, A., Sun, Y. & Sambridge, M. Sea level and global ice volumes from the last glacial maximum to the Holocene. *Proc. Natl Acad. Sci.* **111**, 15296–15303 (2014).

Acknowledgements

We gratefully thank the professional support of the captain and crew of RV Araon on the expedition ARA04C in 2013. We acknowledge Lloyd D. Keigwin for providing study material from core JPC15. We thank Walter Luttmer for conducting Rock-Eval pyrolysis. Thanks to Vera Meyer for input and laboratory support. Furthermore, we thank Torben Gentz, Elizabeth Bonk, and Maylin Malter for radiocarbon analyses. We acknowledge the Alfred Wegener Institute Helmholtz Center for Polar and Marine Research (AWI) and China Scholarship Council for financial support. This work contributes to PALMOD, the German Paleomodelling Research Project funded by BMBF. This research is also supported by the Basic Core Technology Development Program for the Oceans and the Polar Regions (Grant NRF-2021M1A5A1075512 to S.N.) from the National Research Foundation of Korea funded by the Ministry of Science and ICT (MSIT).

Author contributions

R.S. and G.M. designed this study. S.N. performed field work and sampling and provided the X-Ray digital photographs. J.W. carried out biomarker analyses, pre-treatment of bulk OC, and identification of foraminifers. J.H. conducted purification and separation of HMW-FAs. G.M. and H.G. performed AMS¹⁴C analyses and ¹⁴C data processing. R.S. provided and evaluated the Rock-Eval pyrolysis data. P.K. estimated the carbon release and performed carbon cycle modeling. J.W. wrote the manuscript with input from G.M., R.S., K.F., and B.W. All co-authors contributed to the manuscript at different stages.

Funding

Open Access funding enabled and organized by Projekt DEAL.

Competing interests

The authors declare no competing interests.

Additional information

Supplementary information The online version contains supplementary material available at <https://doi.org/10.1038/s41467-022-34725-4>.

Correspondence and requests for materials should be addressed to Junjie Wu, Gesine Mollenhauer or Ruediger Stein.

Peer review information *Nature Communications* thanks Thomas Blattmann, Xingqian Cui and the other, anonymous, reviewer for their contribution to the peer review of this work. Peer reviewer reports are available.

Reprints and permissions information is available at <http://www.nature.com/reprints>

Publisher's note Springer Nature remains neutral with regard to jurisdictional claims in published maps and institutional affiliations.

Open Access This article is licensed under a Creative Commons Attribution 4.0 International License, which permits use, sharing, adaptation, distribution and reproduction in any medium or format, as long as you give appropriate credit to the original author(s) and the source, provide a link to the Creative Commons license, and indicate if changes were made. The images or other third party material in this article are included in the article's Creative Commons license, unless indicated otherwise in a credit line to the material. If material is not included in the article's Creative Commons license and your intended use is not permitted by statutory regulation or exceeds the permitted use, you will need to obtain permission directly from the copyright holder. To view a copy of this license, visit <http://creativecommons.org/licenses/by/4.0/>.

© The Author(s) 2022

Supplementary Information for
**Deglacial release of petrogenic and permafrost carbon from the Canadian
Arctic impacting the carbon cycle**

Junjie Wu*, Gesine Mollenhauer*, Ruediger Stein*, Peter Köhler, Jens Hefter, Kirsten Fahl,
Hendrik Grotheer, Bingbing Wei, Seung-Il Nam

*Corresponding author: junjie.wu@awi.de (J.W.); gesine.mollenhauer@awi.de (G.M.);
rstein@marum.de (R.S.)

This PDF file includes:

Supplementary Discussion Texts 1 and 2

Supplementary Figures 1 to 8

Supplementary Tables 1 and 2

Supplementary Discussion

Text 1: Mixing model and endmember values

Mixing model

A three-endmember mixing model based on $\delta^{13}\text{C}_{\text{org}}$ and F^{14}C signature was used to estimate fractional contributions of $\text{OC}_{\text{marine-bio}}$ ($f_{\text{marine-bio}}$), $\text{OC}_{\text{terr-bio}}$ ($f_{\text{terr-bio}}$), and OC_{petro} (f_{petro}), assuming mass-balance:

$$\text{F}^{14}\text{C}_{\text{bulk-ini}} = f_{\text{marine-bio}} \times \text{F}^{14}\text{C}_{\text{marine-bio}} + f_{\text{terr-bio}} \times \text{F}^{14}\text{C}_{\text{terr-bio}} + f_{\text{petro}} \times \text{F}^{14}\text{C}_{\text{petro}} \quad (1)$$

$$\delta^{13}\text{C}_{\text{bulk}} = f_{\text{marine-bio}} \times \delta^{13}\text{C}_{\text{marine-bio}} + f_{\text{terr-bio}} \times \delta^{13}\text{C}_{\text{terr-bio}} + f_{\text{petro}} \times \delta^{13}\text{C}_{\text{petro}} \quad (2)$$

$$1 = f_{\text{marine-bio}} + f_{\text{terr-bio}} + f_{\text{petro}} \quad (3)$$

The $\delta^{13}\text{C}_{\text{bulk}}$ and $\text{F}^{14}\text{C}_{\text{bulk-ini}}$ denote the values of analyzed bulk sediments. In this case, the $\text{F}^{14}\text{C}_{\text{bulk-ini}}$ refers to fraction modern carbon before deposition ($\text{F}^{14}\text{C}_{\text{initial}} = \text{F}^{14}\text{C} \times e^{\lambda t}$, t is the time since deposition). The $\delta^{13}\text{C}_{\text{bulk}}$ is directly measured in sediment samples. Other isotope values are source characteristics (the definition of each endmember value is explained below).

To obtain correct estimates, a Markov chain Monte Carlo Bayesian approach (MCMC) was applied to include uncertainty of source-signature $\delta^{13}\text{C}$ and F^{14}C , minimizing errors from arbitrary assignments of endmember values. Analytical errors of the samples are not included in the mixing model, as they are considered negligible compared to the endmember uncertainties. The simulation was performed on MATLAB, based on the script from Andersson et al. (2015)¹. Briefly, 1,000,000 out of 100,000,000 random data from the normal distribution of each endmember within the given mean and standard deviation were taken to simultaneously fulfill the given system in simulations. The mean relative contributions and the standard deviation of different OC pools were then estimated.

Endmembers

Marine biospheric carbon

Since no proper $\delta^{13}\text{C}$ and F^{14}C data from local phytoplankton are available, $\delta^{13}\text{C}_{\text{marine-bio}}$ is defined as $-24.0 \pm 1.0\%$, using data from the Siberian Arctic shelf². $\text{F}^{14}\text{C}_{\text{marine-bio}}$ largely depends on the radiocarbon content of dissolved inorganic carbon (DIC) in surface waters.

Thus, $F^{14}C_{\text{marine-bio}}$ has been assumed the same as $F^{14}C_{\text{surface}}$ (fraction modern carbon of DIC in surface waters). The marine reservoir age R indicates the offset metric between the ^{14}C contents of reservoirs of the ocean surface and the atmosphere, which can be expressed as the Supplementary Eq.4³:

$$R = -8033 \times \ln \frac{F^{14}C_{\text{surface}}}{F^{14}C_{\text{atmosphere}}} \quad (4)$$

Hence, $F^{14}C_{\text{surface}}$ ($F^{14}C_{\text{marine-bio}}$) has been derived based on the $F^{14}C_{\text{atmosphere}}$ from IntCal13⁴ and the regional marine reservoir age R . Note that $F^{14}C_{\text{atmosphere}}$ varies through time, and thus a variable $F^{14}C_{\text{marine-bio}}$ is used in the mixing model. R in high latitudes might be larger than the global average (405 years) due to the sea ice impact and is simulated to be 1000 years in the Canadian Beaufort Sea⁵. In the nearby regions of the western Arctic Ocean, ΔR has been determined to be 440 ± 101 years in the Chukchi/Beaufort, 350 ± 116 years in the Amundsen Gulf, and 286 ± 74 years in the Foxe Basin (cf., ref⁶). Collectively, the regional R in the Canadian Beaufort Sea appears to range between 405-1000 years. In order to validate the robustness of our mixing model, both $F^{14}C_{\text{marine-bio}}$ values derived from scenarios of $R=405$ years and $R=1000$ years are tested in the model (see below). Additionally, due to the ocean circulation change, the sea surface reservoir ages were 200 years greater during the YD⁷. Thus, the regional $R=605$ and $R=1200$ are used for the YD period. Figure 4b shows the variable $F^{14}C_{\text{marine-bio}}$ that we used in the mixing model (based on the scenario of $R=405$ years).

Uncertainties (σ) on reservoir age offset R are functions of the $F^{14}C$ values of two reservoirs and their associated uncertainties³:

$$\sigma_R = 8033 \times \sqrt{\left(\frac{\sigma_{\text{surface}}}{F^{14}C_{\text{surface}}}\right)^2 + \left(\frac{\sigma_{\text{atmosphere}}}{F^{14}C_{\text{atmosphere}}}\right)^2} \quad (5)$$

Here we assume an uncertainty of 100 years for the reservoir age R (to keep consistency with the uncertainties used in the age model) and derive the uncertainties of $F^{14}C_{\text{surface}}$ ($F^{14}C_{\text{marine-bio}}$).

Terrestrial biospheric carbon

The majority of terrestrial OC delivered to the study site is discharged from the Mackenzie River. In this study, source characteristics from Herschel Island and Yukon Coast have been considered as well since these regions are characterized by high erosion rates and may contribute to significant terrestrial carbon release. A study of soil organic carbon on a north-south transect in western Canada (including the Mackenzie River basin) suggests a mean $\delta^{13}\text{C}_{\text{terr-bio}}$ value of $-26.2 \pm 0.5\%$ ⁸. Analysis of samples from the Herschel Island retrogressive thaw slumps (n=7) and onshore samples from the Yukon Coastal Plain (n=19) gives a mean $\delta^{13}\text{C}_{\text{terr-bio}}$ value of $-26.5 \pm 0.3\%$ ^{9,10}, which is within the range reported by Bird et al. (2002)⁸. Therefore, the endmember $\delta^{13}\text{C}$ value of terrestrial biospheric carbon is defined as $-26.2 \pm 0.5\%$ in our mixing model.

Defining the endmember $F^{14}\text{C}$ value of terrestrial biospheric carbon needs to consider the dynamics of ice sheets, permafrost formation, and vegetation development during the ice sheet retreat. In this context, the relatively fixed endmember values from the contemporary system are not representative of these changes and thus might not be applicable to the paleo system. Instead, HMW n-alkanoic acids derived from the study material can to some degree reflect the dynamic changes for different periods. Besides, using HMW n-alkanoic acids relieves the constraint of finding proper endmember values to represent all possible sources. One should also consider that the endmember values determined on bulk OC on land are fixed while the radiocarbon signals of terrestrial OC delivered to the study site may change (e.g., become depleted) via preferential degradation or re-suspension during transport, and such biases may eventually cause an underestimate of $\text{OC}_{\text{terr-bio}}$ contribution. In contrast, using HMW n-alkanoic acids values determined from the study site circumvents these additional complications. Hence, we define the $F^{14}\text{C}$ of HMW-FAs (corrected for depositional decay) as endmember values of terrestrial biospheric carbon.

Petrogenic organic carbon

OC_{petro} is radiocarbon free and the endmember $F^{14}\text{C}_{\text{petro}}$ is defined as 0. Unfortunately, studies on the stable carbon isotopic composition of OC_{petro} are scarce in the Mackenzie River basin. Hence, we turn to the nearby regions to obtain representative endmember $\delta^{13}\text{C}$ values.

There are three geological units in the Mackenzie River catchment: North American Cordillera, the Interior Platform, and the Canadian Shield. The North American Cordillera and central Interior Platform are likely the major contributors of OC_{petro} ¹¹. According to the geological map

of Canada, the two geological units in the catchment mainly include Phanerozoic sedimentary rocks, more specifically Cambrian to Cretaceous strata. Records from Alberta¹² can serve to provide information on the characteristics of sedimentary rocks from the Interior Platform, while records from British Columbia^{13,14} can provide constraints on sedimentary rocks from the Cordillera. These records have further been placed in a global compilation and are consistent with the $\delta^{13}\text{C}$ values of kerogens from various Phanerozoic sedimentary rocks¹⁵ (Supplementary Fig. 3).

The $\delta^{13}\text{C}$ data from Canadian sedimentary rocks gives a mean value of $-29.0 \pm 1.4\%$. However, these records mainly cover the Permian to Jurassic. Therefore, a mean $\delta^{13}\text{C}$ value of $-28.6 \pm 1.3\%$ of Cambrian to Cretaceous rocks has been calculated from a global compilation¹⁵. Both $\delta^{13}\text{C}$ values have been used to test the robustness of the mixing model output (see below).

Robustness of mixing model

To test the model sensitivity, endmember $F^{14}\text{C}_{\text{marine-bio}}$ values derived from scenarios of $R=405$ years and $R=1000$ years are tested respectively. Endmember values of each scenario are defined as follows:

Scenario 1: $F^{14}\text{C}_{\text{marine-bio}}$ values are derived from the scenario of $R=405$ years, and the $\delta^{13}\text{C}_{\text{petro}}$ value is defined as $-28.6 \pm 1.3\%$. Please see the definitions of other endmember values above.

Scenario 2: $F^{14}\text{C}_{\text{marine-bio}}$ values are derived from the scenario of $R=1000$ years, and the $\delta^{13}\text{C}_{\text{petro}}$ value is defined as $-28.6 \pm 1.3\%$. Please see the definition of other endmember values above.

Under both circumstances, the outcome remains the same (Supplementary Figure 4), indicating that our results are robust within the possible range of R . Therefore, we use $F^{14}\text{C}_{\text{marine-bio}}$ values derived from the scenario of $R=405$ years for the following tests.

The $\delta^{13}\text{C}_{\text{petro}}$ data from both British Columbia and Alberta gives a mean $\delta^{13}\text{C}_{\text{petro}}$ value of $-29.0 \pm 1.4\%$ ($n=436$), which has been tested in Scenario 3.

Scenario 3: $F^{14}\text{C}_{\text{marine-bio}}$ values are derived from the scenario of $R=405$ years, and the $\delta^{13}\text{C}_{\text{petro}}$ value is defined as $-29.0 \pm 1.4\%$. Please see the definitions of other endmember values above.

The model outcome shows negligible differences with using the $\delta^{13}\text{C}_{\text{petro}}$ value from the global compilation (Supplementary Figure 4), suggesting that the results are robust within the possible $\delta^{13}\text{C}_{\text{petro}}$ range.

Because of the less constrained chronology at the top and the base of the core, uncertainties of depositional age should be taken into consideration which may impact the sample $F^{14}C_{\text{bulk-ini}}$ and endmember $F^{14}C_{\text{terr-bio}}$ and may further influence the mixing model output. Note that age biases impact both $F^{14}C_{\text{bulk-ini}}$ and $F^{14}C_{\text{terr-bio}}$, hence uncertainties cannot be simply assigned to the sample $F^{14}C_{\text{bulk-ini}}$ and endmember $F^{14}C_{\text{terr-bio}}$. Instead, we incorporate maximum and minimum depositional ages in the calculation respectively, as indicated in Scenarios 4 and 5.

Scenario 4: Maximum depositional ages are incorporated in the calculation of $F^{14}C_{\text{bulk-ini}}$ and $F^{14}C_{\text{terr-bio}}$. $F^{14}C_{\text{marine-bio}}$ values are derived from the scenario of $R=405$ years, and the $\delta^{13}C_{\text{petro}}$ value is defined as $-28.6\pm 1.3\%$. Please see the definitions of other endmember values above.

Scenario 5: Minimum depositional ages are incorporated in the calculation of $F^{14}C_{\text{bulk-ini}}$ and $F^{14}C_{\text{terr-bio}}$. $F^{14}C_{\text{marine-bio}}$ values are derived from the scenario of $R=405$ years, and the $\delta^{13}C_{\text{petro}}$ value is defined as $-28.6\pm 1.3\%$. Please see the definitions of other endmember values above.

The outcome of Scenarios 4 and 5 illustrates a negligible influence of age model uncertainties (Supplementary Figure 4).

Overall, the exercises demonstrate a robust mixing model outcome. Different scenarios have negligible influence on our estimate. As the mixing model output remains nearly the same in all scenarios, we discuss in the Main Text based on the mixing model outcome of Scenario 1 which is shown in Supplementary Table 1.

Text 2: Mass accumulation rates of organic carbon

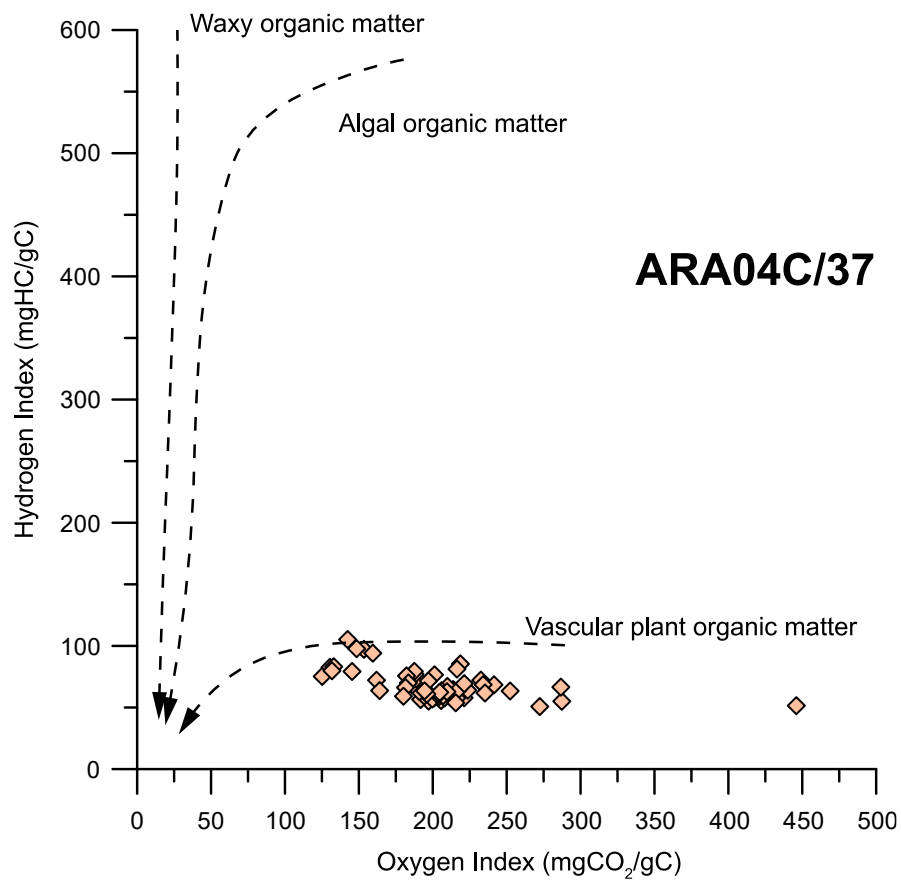
Changes in OC_{petro} MARs are used in the Main Text to reflect changes in OC_{petro} oxidation flux. Since our mixing model provides a robust outcome of source fractions of OC_{petro} , defining TOC MARs becomes crucial for estimating OC_{petro} MARs. TOC MARs show three distinct peaks between 14-10 cal. kyr BP (Fig. 3d), triggered by the YD flood event and two more events of coastal erosion. In addition to the influence of these strong events, the sharp increase in TOC MARs may be partially driven by the limited dating points in the age model. It implies that using TOC MARs from these intervals may cause an overestimate of OC_{petro} MARs.

In this context, for samples deposited between 10-0 cal. kyr BP, the samples' respective TOC MARs are used to calculate OC_{petro} MARs. However, for samples deposited between 14-10 cal. kyr BP, we tested three scenarios using different TOC MARs. In a conservative estimate, the

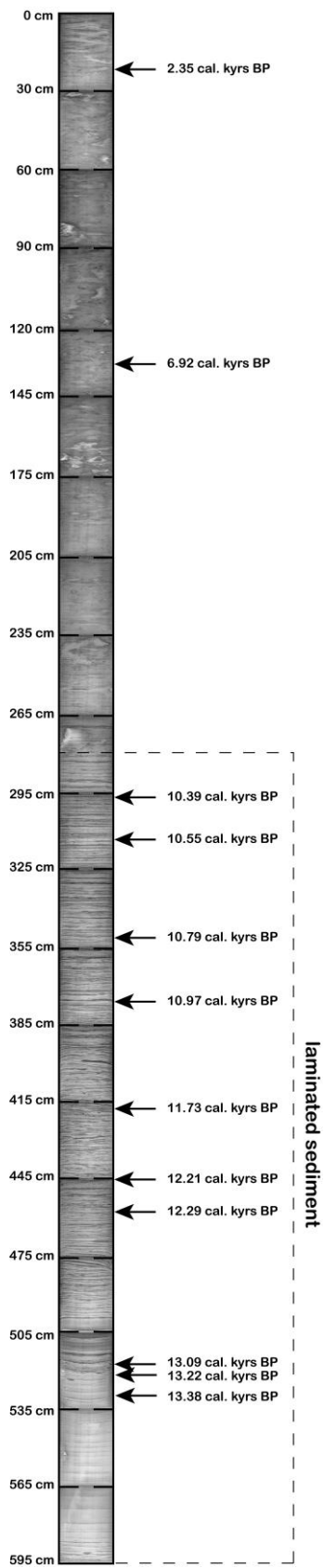
average value of low TOC MARs (values in between events) between 14-10 cal. kyr BP is used to estimate OC_{petro} MARs (Supplementary Figure 5a). In the second scenario, the average TOC MAR derived from the entire period of 14-10 cal. kyr BP is used (Supplementary Figure 5b). In scenario 3, the samples' respective TOC MARs are used (Supplementary Figure 5c).

The OC_{petro} MARs discussed in the Main Text are calculated from a conservative estimate of TOC MARs.

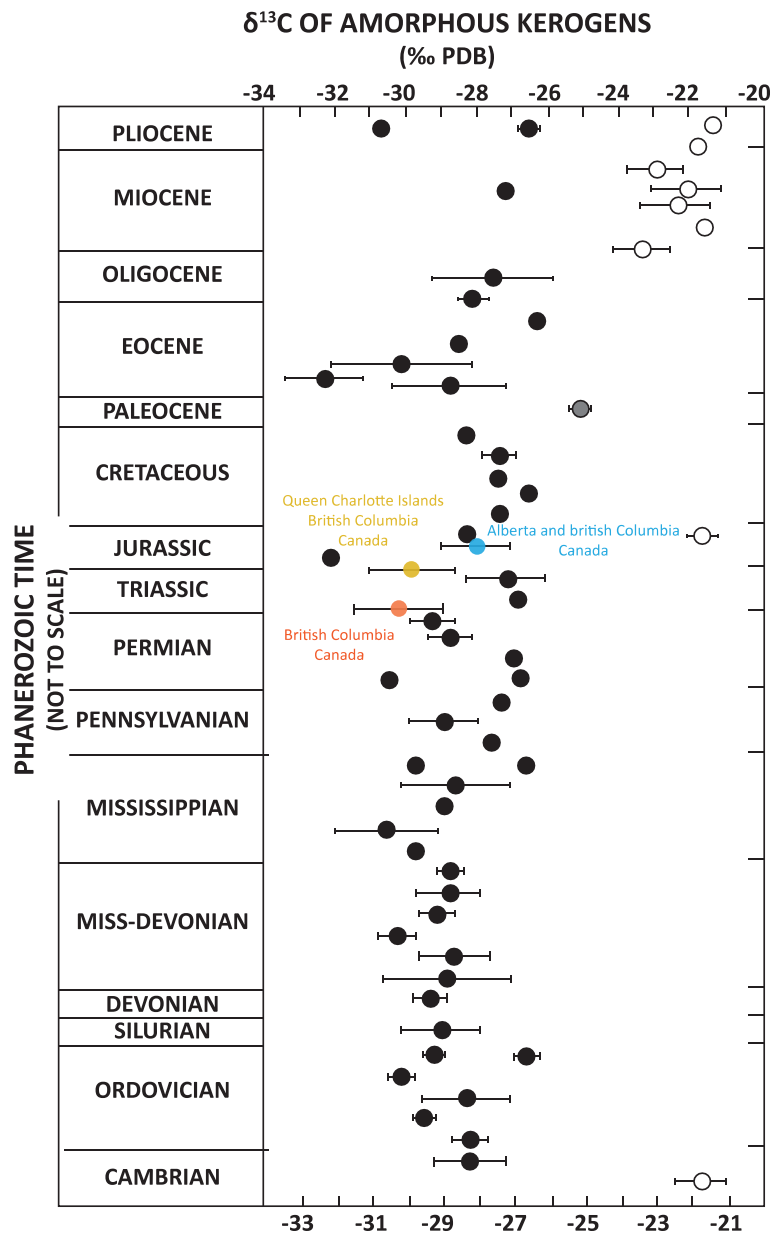
Supplementary Figures



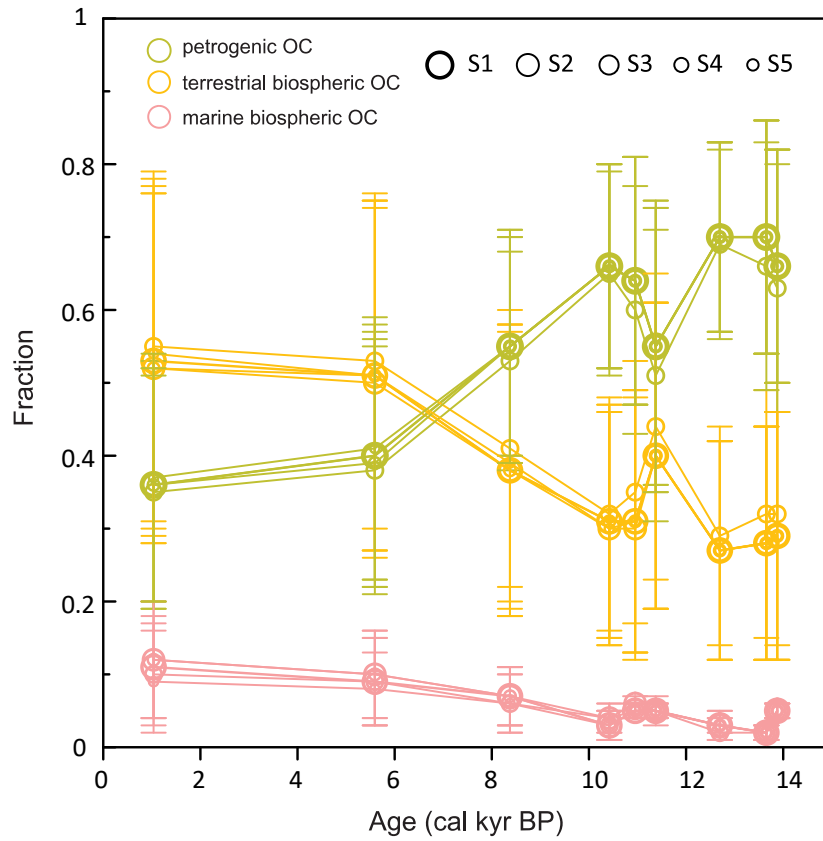
Supplementary Figure 1. Carbon sources based on pyrolysis. The pseudo van Krevelen-type diagram shows hydrogen index and oxygen index for bulk OC. The dashed lines illustrate different carbon sources (cf., ref¹⁶).



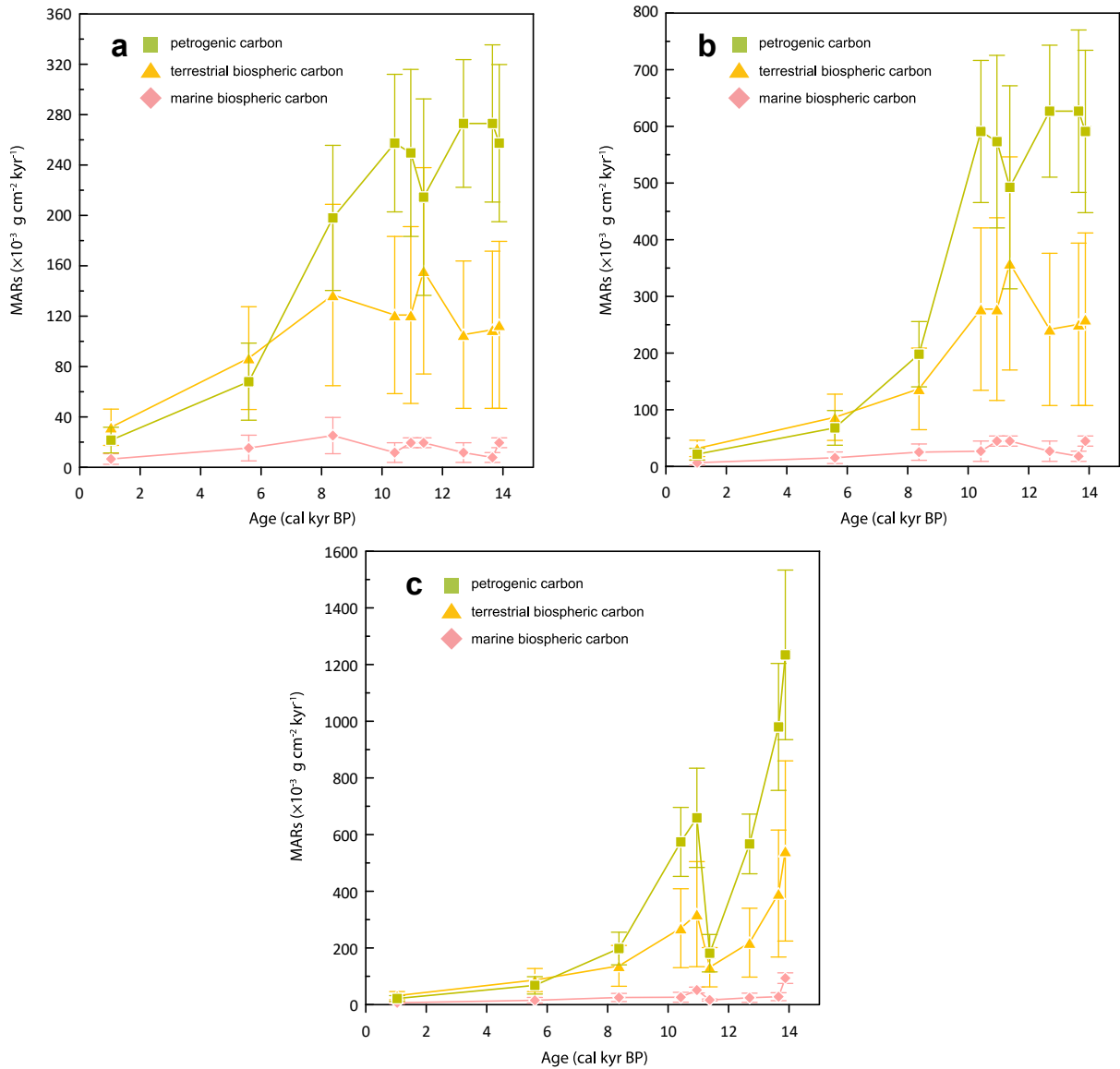
Supplementary Figure 2. Lithology of core ARA04C/37. X-ray digital radiograph showing lithology and sedimentary texture (bioturbation and lamination) of core ARA04C/37.



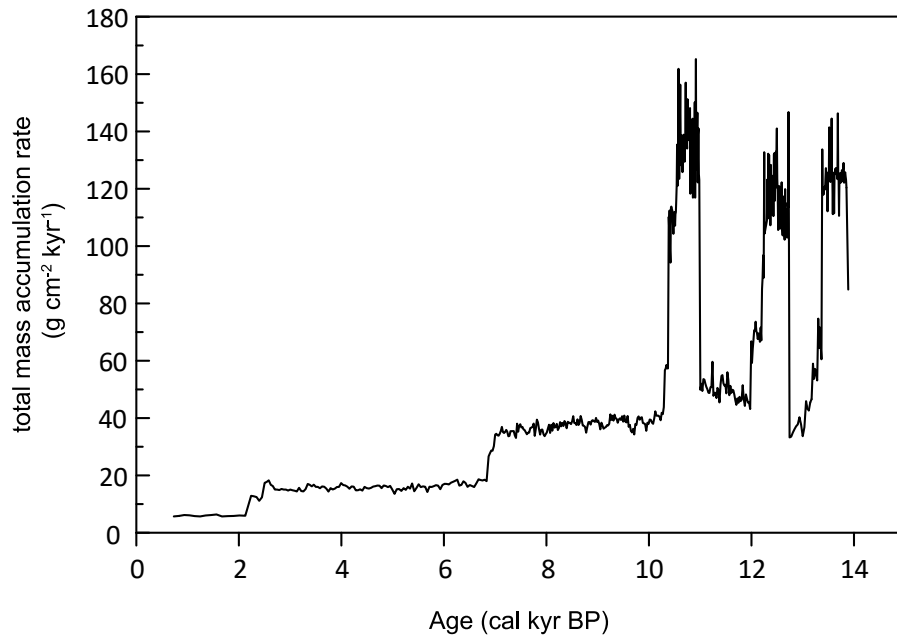
Supplementary Figure 3. stable carbon isotopes of kerogens from Phanerozoic rock units. Colour circles indicate the stable isotope composition of rocks from Canada¹²⁻¹⁴. White circles denote *h*-amorphous kerogens, and black circles denote *l*-amorphous kerogens from various regions¹⁵. Error bars represent standard deviation.



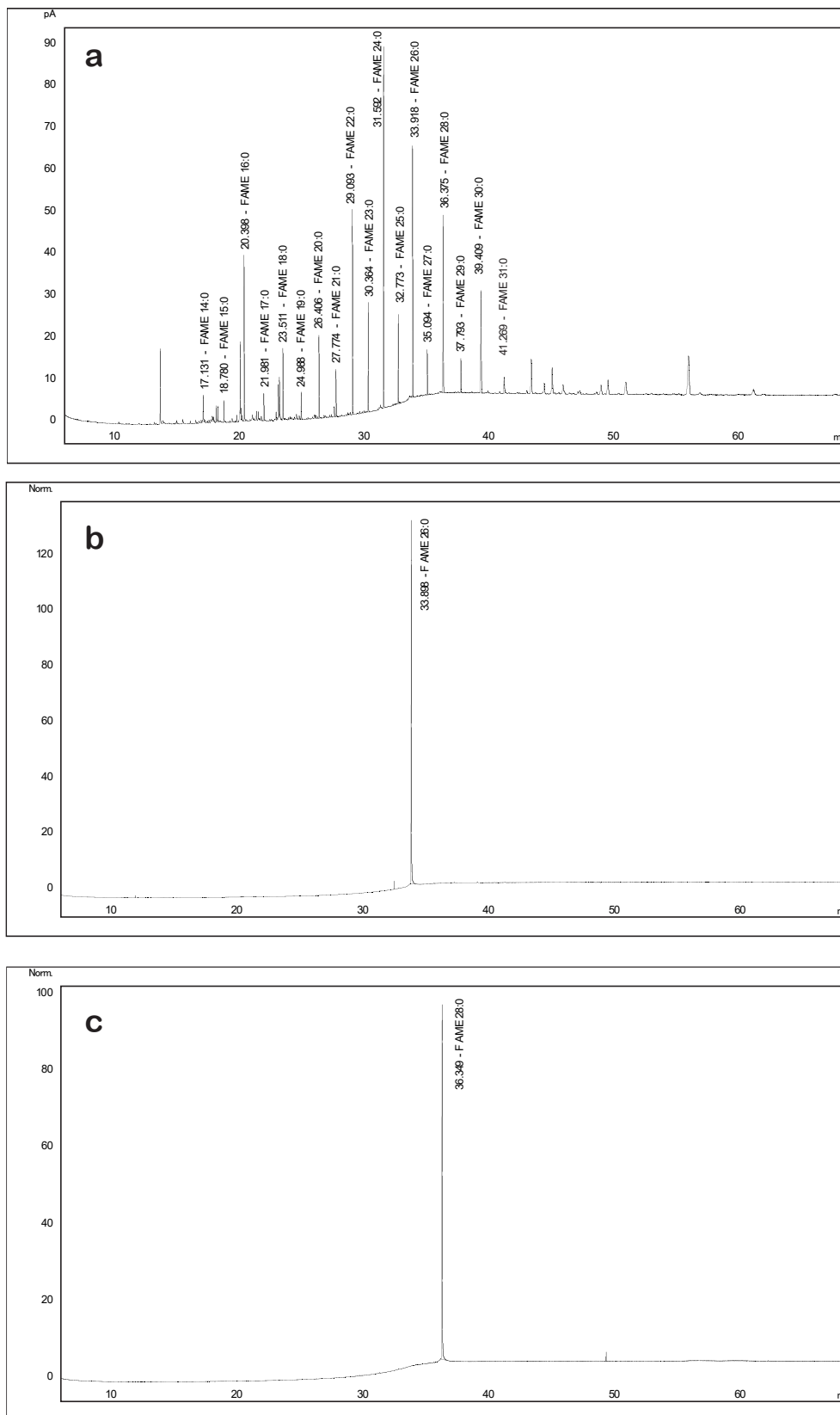
Supplementary Figure 4. Mixing model sensitivity. The plots show the results of source apportionments for samples in core ARA04C/37. Different sizes of circles indicate the results of scenarios 1-5 (S1-S5) discussed in Supplementary Discussion Text 1. Error bars represent standard deviation.



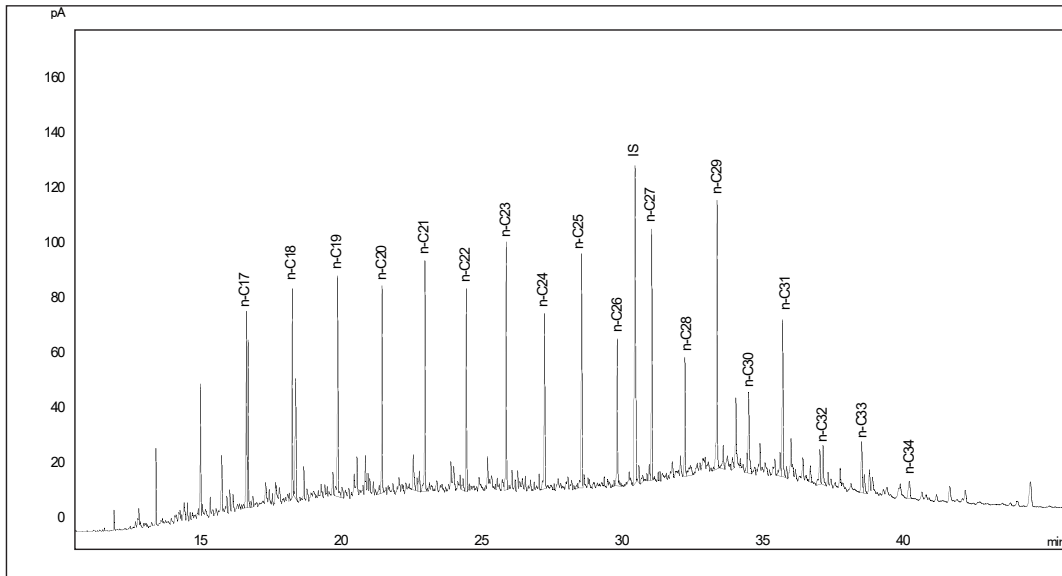
Supplementary Figure 5. Mass accumulation rates (MARs) of different types of carbon. a-c show the MARs of OC_{petro} , $OC_{\text{terr-bio}}$, and $OC_{\text{marine-bio}}$. In **a** and **b**, MARs between 14-10 cal. kyr BP are calculated based on an average value of low TOC MARs (values in between events of high MAR – see Figure 3d) (**a**) and an average TOC MAR from the entire period of 14-10 cal. kyr BP (**b**), while in panel **c** MARs are calculated based on samples' respective TOC MARs (Supplementary Discussion Text 2). Error bars represent standard deviation.



Supplementary Figure 6. Total mass accumulation rates of ARA04C/37. The total mass accumulation rates are updated from Wu et al. (2020)¹⁷ by including two more AMS¹⁴C dates (Supplementary Table 2).



Supplementary Figure 7. Representative chromatograms of *n*-alkanoic acids in core ARA04C/37. a representative chromatogram of *n*-alkanoic acids. **b-c** representative chromatograms of C_{26:0} and C_{28:0} fatty acids that are used for compound-specific radiocarbon analyses.



Supplementary Figure 8. Representative chromatogram of an *n*-alkanes fraction extracted from sediments of core ARA04C/37. IS denotes the internal standard squalane.

Supplementary Tables

Supplementary Table 1. Source fractions of marine biospheric carbon, terrestrial biospheric carbon, and petrogenic organic carbon, based on a three-endmember mixing model.

Depth (cm)	Age (cal. kyr BP)	Marine biospheric carbon (mean±s.d.)	Terrestrial biospheric carbon (mean±s.d.)	Petrogenic organic carbon (mean±s.d.)
9	1.036	0.11±0.07	0.53±0.24	0.36±0.17
99	5.592	0.09±0.06	0.51±0.24	0.40±0.18
199	8.374	0.07±0.04	0.38±0.20	0.55±0.16
299	10.420	0.03±0.02	0.31±0.16	0.66±0.14
372	10.952	0.05±0.01	0.31±0.18	0.64±0.17
399	11.376	0.05±0.01	0.40±0.21	0.55±0.20
499.5	12.695	0.03±0.02	0.27±0.15	0.70±0.13
564	13.653	0.02±0.01	0.28±0.16	0.70±0.16
593	13.877	0.05±0.01	0.29±0.17	0.66±0.16

Supplementary Table 2. AMS¹⁴C dates of core ARA04C/37

Lab ID	Depth (cm)	Species	AMS ¹⁴ C age (year)	ΔR	Calibrated age* (cal. year BP)	Model age** (cal. year BP)
6472.1.2	521	planktic	11756±101	0±100	13233±140	13220±123
6474.1.2	530	planktic	12095±104	0±100	13553±154	13381±157

AMS¹⁴C dating of the core ARA04C/37 has been carried out at the Alfred Wegener Institute Bremerhaven using the Mini Carbon Dating System (MICADAS)¹⁸.

*Calibrated ages with 1σ uncertainty, using Calib 7.1¹⁹ and based on calibration curve Marine13⁴.

**model ages with default 95% confidence ranges based on Bayesian model (Bacon)²⁰ and Marine13⁴ in this study.

Supplementary References

1. Andersson, A. *et al.* Regionally-Varying Combustion Sources of the January 2013 Severe Haze Events over Eastern China. *environmental science & Technology* **49**, 2038–2043 (2015).
2. Vonk, J. E. *et al.* Preferential burial of permafrost-derived organic carbon in Siberian-Arctic shelf waters. *Journal of Geophysical Research: Oceans* **119**, 8410–8421 (2014).
3. Soulet, G., Skinner, L. C., Beaupré, S. R. & Galy, V. A note on reporting of reservoir ^{14}C disequilibria and age offsets. *Radiocarbon* **58**, 205–211 (2016).
4. Reimer, P. J. *et al.* Intcal13 and Marine13 Radiocarbon Age Calibration Curves 0–50,000 Years Cal Bp. *Radiocarbon* **55**, 1869–1887 (2013).
5. Butzin, M., Köhler, P. & Lohmann, G. Marine radiocarbon reservoir age simulations for the past 50,000 years. *Geophysical Research Letters* **44**, 8473–8480 (2017).
6. Keigwin, L. D. *et al.* Deglacial floods in the Beaufort Sea preceded Younger Dryas cooling. *Nature Geoscience* **11**, 599–604 (2018).
7. Bondevik, S., Mangerud, J., Birks, H. H., Gulliksen, S. & Reimer, P. Changes in North Atlantic Radiocarbon Reservoir Ages During the Allerød and Younger Dryas. *Science* **312**, 1514–1517 (2006).
8. Bird, M., Santrůcková, H., Lloyd, J. & Lawson, E. The isotopic composition of soil organic carbon on a north-south transect in western Canada. *European Journal of Soil Science* **53**, 393–403 (2002).
9. Grotheer, H. *et al.* Burial and origin of permafrost derived carbon in the nearshore zone of the southern Canadian Beaufort Sea. *Geophysical Research Letters* **47**, e2019GL085897 (2020).
10. Couture, N. J., Irrgang, A., Pollard, W., Lantuit, H. & Fritz, M. Coastal Erosion of Permafrost Soils Along the Yukon Coastal Plain and Fluxes of Organic Carbon to the Canadian Beaufort Sea. *Journal of Geophysical Research: Biogeosciences* **123**, 406–422 (2018).
11. Campeau, A., Soerensen, A., Martma, T., Åkerblom, S. & Zdanowicz, C. Controls on the ^{14}C -content of dissolved and particulate organic carbon mobilized across the Mackenzie River basin, Canada. *Global Biogeochemical Cycles* **34**, e2020GB006671 (2020).
12. Them, T. R. *et al.* High-resolution carbon isotope records of the Toarcian Oceanic Anoxic Event (Early Jurassic) from North America and implications for the global drivers of the Toarcian carbon cycle. *Earth and Planetary Science Letters* **459**, 118–126 (2017).
13. Wang, K., Geldsetzer, H. H. J. & Krouse, H. R. Permian-Triassic extinction: Organic $\delta^{13}\text{C}$ evidence from British Columbia, Canada. *Geology* **22**, 580–584 (1994).
14. Williford, K. H., Ward, P. D., Garrison, G. H. & Buick, R. An extended organic carbon-isotope record across the Triassic-Jurassic boundary in the Queen Charlotte Islands, British Columbia, Canada. *Palaeogeography, Palaeoclimatology, Palaeoecology* **244**, 290–296 (2007).
15. Lewan, M. D. Stable carbon isotopes of amorphous kerogens from Phanerozoic sedimentary rocks. *Geochimica et Cosmochimica Acta* **50**, 1583–1591 (1986).
16. Tissot, B. P. & Welte, D. H. *Petroleum Formation and Occurrence*. (Springer-Verlag, 1984).

17. Wu, J. *et al.* Deglacial to Holocene variability in surface water characteristics and major floods in the Beaufort Sea. *Communications Earth & Environment* **1**, 27 (2020).
18. Mollenhauer, G., Grotheer, H., Gentz, T., Bonk, E. & Hefter, J. Standard operation procedures and performance of the MICADAS radiocarbon laboratory at Alfred Wegener Institute (AWI), Germany. *Nuclear Instruments and Methods in Physics Research, Section B: Beam Interactions with Materials and Atoms* **496**, 45–51 (2021).
19. Stuiver, M., Reimer, P. J. & Reimer, R. W. CALIB 7.1 [WWW program] at <http://calib.org>. (2020).
20. Blaauw, M. & Christeny, J. A. Flexible paleoclimate age-depth models using an autoregressive gamma process. *Bayesian Analysis* **6**, 457–474 (2011).